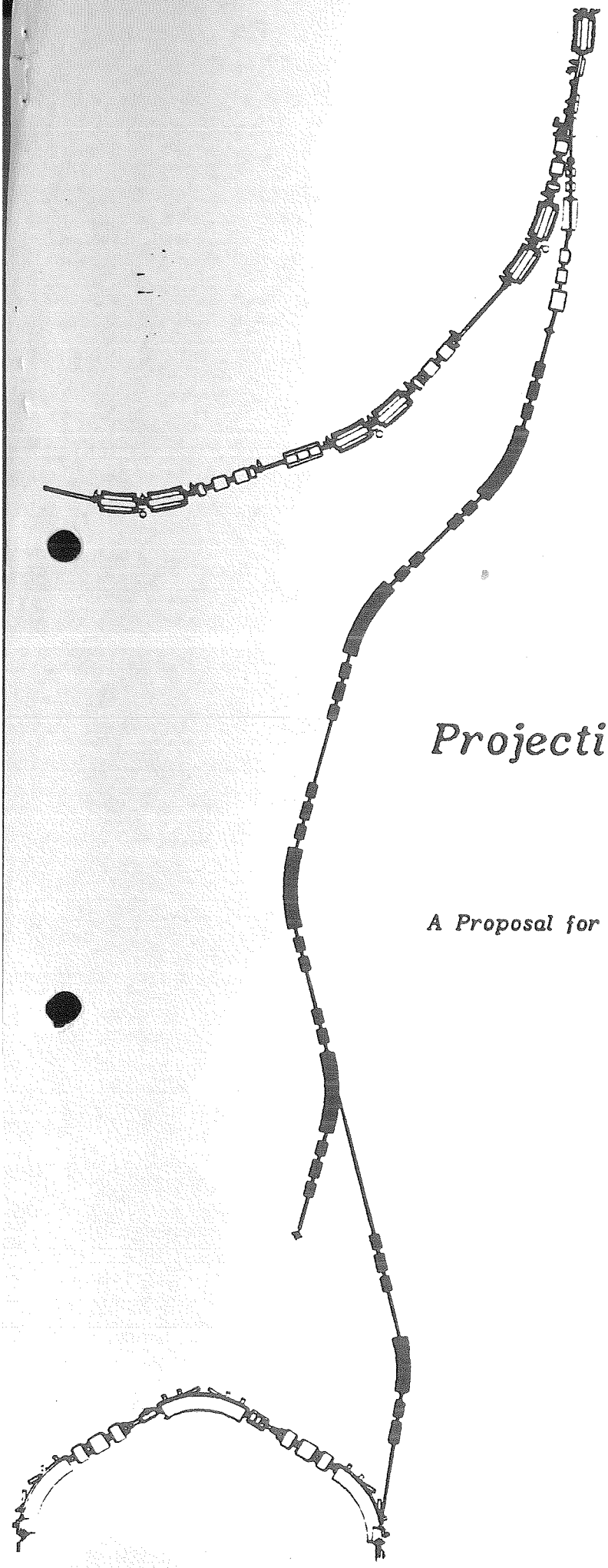

Projectile Fragment Separator

A Proposal for the SIS-ESR Experimental Programme

PROJECTILE-FRAGMENT SEPARATOR

A Proposal for the SIS-ESR Experimental Programme

H. Geissel, P. Armbruster, B. Franczak, B. Langenbeck,
O. Klepper, F. Nickel
E. Roeckl, D. Schardt, K.-H. Schmidt, D. Schüll, K. Sümmerer,
and G. Münzenberg
GSI Darmstadt

J.P. Dufour, M. S. Pravikoff
C.E.N. Bordeaux

H.-G. Clerc, E. Hanelt
TH Darmstadt

T. Schwab, H. Wollnik
Univ. Giessen

B. Sherrill
Michigan State University

Darmstadt, February 1987

1. Introduction

The heavy-ion synchrotron (SIS) presently under construction at GSI (fig. 1.1) will provide high-intensity beams of relativistic heavy ions. Secondary beams of radioactive nuclei can be produced by projectile fragmentation and electromagnetic dissociation. With the beam currents planned for SIS we expect radioactive beams with intensities of up to 5×10^8/s for isotopes close to the projectile, and production rates still sufficient for nuclear spectroscopy at the borderlines of known nuclei.

The projectile fragments are emitted in forward direction with velocities close to the projectiles, so they can be separated in-flight and injected into the storage ring (ESR). The proposed separator for projectile fragments (FRS) at GSI is planned to separate in-flight nuclides up to uranium in A and Z at specific energies in the range of 0.1 to 1.0 GeV/u. The limitation for the separation of short-lived fragments is given by the time-of-flight through the separator, which is of the order of 300 ns. The separator combines the isotopic separation of ISOLDE-type separators with the short separation time and the versatility for all nuclei of the recoil separators. Due to this unique properties the proposed separator is expected to open up a new area of research. The principle of the separation of single isotopes is based on a combination of magnetic analysis and electronic energy loss of the fragments in a degrader. Therefore the separation characteristics are determined by the magnetic separation system and by the interactions of fragments penetrating through matter.

The separated fragments can be implanted into detector telescopes for nuclear spectroscopy or into solids and biological samples for studies in material science and applied research. A new generation of exciting experiments is offered with radioactive beams injected into the ESR where they can be cooled and used, e.g., for investigations of the nuclear decay of highly stripped ions, direct mass measurements with the circulating beams, or nuclear spectroscopy via reaction studies with internal targets in inverse kinematics. A deceleration in the ESR down to the Coulomb barrier is also possible. In this case the cooling-time in the storage ring restricts the minimum life-time of the fragments to about 1 s. The stored ions can also be extracted and sent to the target hall, to provide exotic beams with low emittance in the energy range from 3 to 500 MeV/u.

The aim of this paper is to propose a separator for relativistic projectile fragments and not to propose a complete experimental programme for the device. We give a description of the principles of the new separation method and of the separator itself.

as well as of its ion-optical design and the storage of radioactive beams in the ESR. The parameters reflect the present status of the project and may still be subject to modifications.

We present some exemplary experiments, in order to stimulate discussions in this field. Some detailed proposals are presented separately and more are expected in the future. The first experimental programme should be subject of a forthcoming workshop of the future users of the FRS.

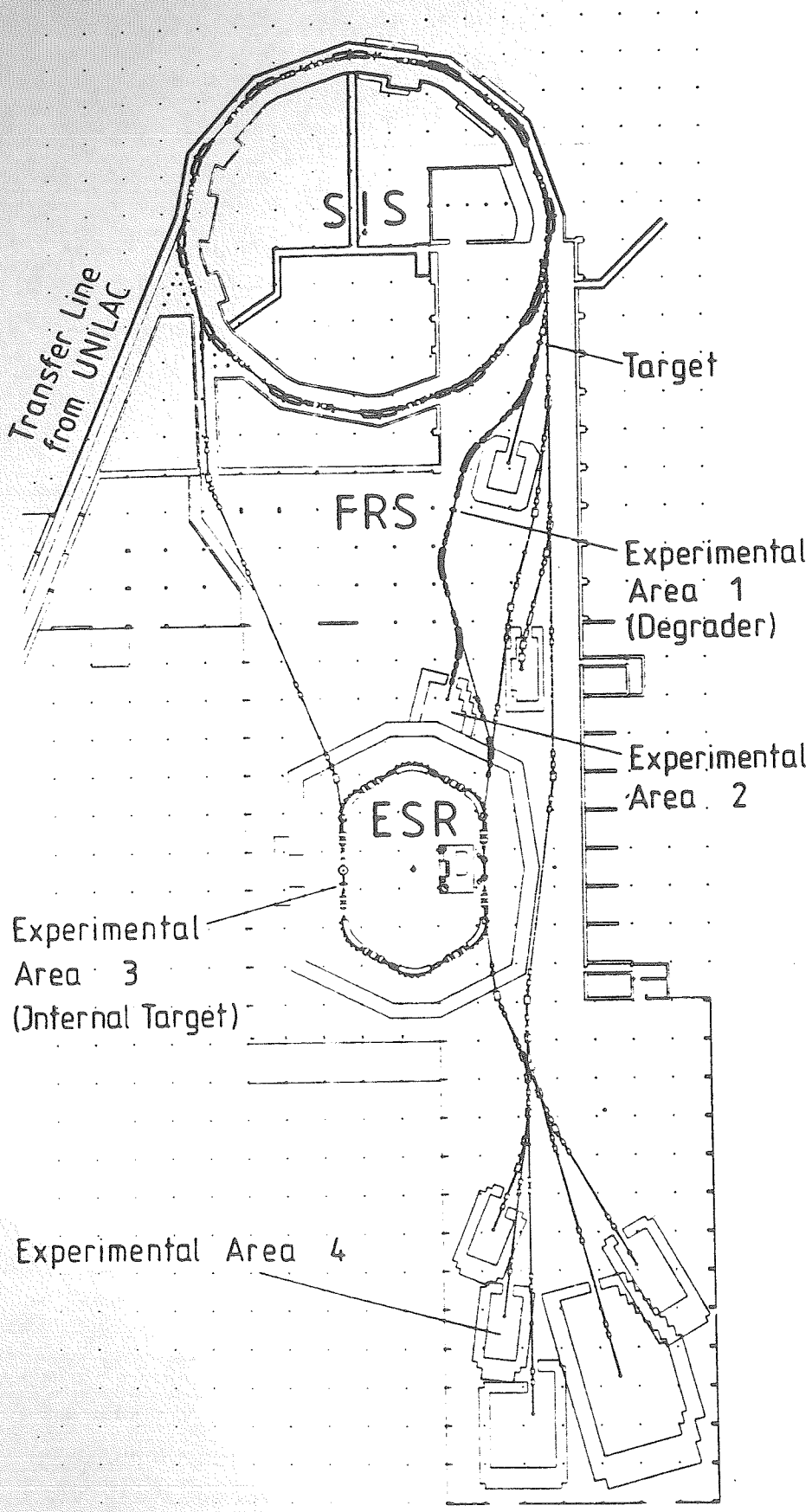

Fig. 1.1: Layout of the SIS/ESR accelerator complex and experimental areas together with the Fragment Separator FRS located between the two rings.

2. Scientific Motivation

2.1. Experiments with the Projectile Fragment Separator

The fragment separator will be optimized to separate efficiently projectile fragments with respect to A and Z. Furthermore the different dipole sections of the FRS may be used to prepare beams with well-defined charge states. Experiments which can be performed directly at the separator are: decay spectroscopy of nuclei far from stability, studies of ground state properties of exotic nuclei, spectroscopy of few-electron systems, investigations of atomic collisions with few-electron ions, measurements on the slowing-down and charge exchange of relativistic ions in matter and applications in other fields of science. The magnetic system can also be operated as a high-resolution energy-loss spectrometer (see Sec. 5), which might offer advantages for reaction studies with a target positioned at the intermediate focal plane. Independent of the relatively large momentum spread of the incident projectile beams [SCH64], high resolution measurements of the energy transfer in nuclear reactions become possible. All these experiments may be performed with the separator in 'stand-alone' operation.

A new generation of experiments will be possible with the combination of SIS, the fragment separator FRS, and the storage ring ESR. The separated fragments can be stored, cooled and investigated in the ring. For example, accumulated fragments of high phase-space density allow to study their nuclear structure in inelastic collisions with light internal target atoms (H,D,^{3}He). Measurements of β-decay into bound final electron states can be systematically performed for the first time [BOS86a]. FRS in combination with the ESR will be a unique tool for direct mass measurements of exotic nuclei up to Z = 92.

2.1.1. Nuclear Physics Experiments

The scientific motivation for nuclear physics experiments with exotic nuclei is a straightforward continuation at SIS-ESR of the successful programme of the investigations of exotic nuclei during the past ten years of heavy ion research at the UNILAC [ANG86]. In particular, the spectroscopy of numerous new isotopes (see fig. 2.1) gave interesting information on the nuclear structure far from the valley of stability.

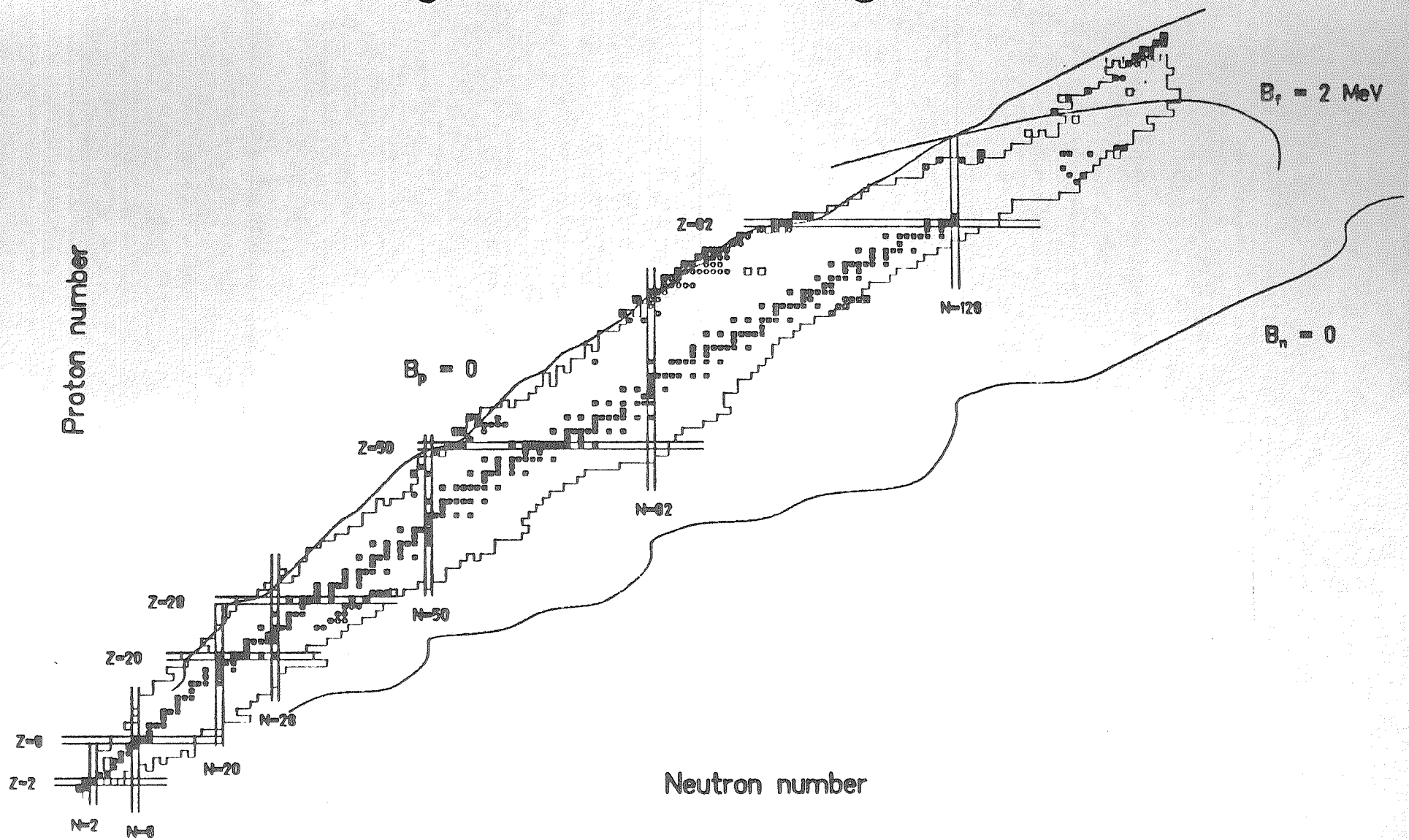

Fig. 2.1: Chart of the nuclides indicating stable nuclei (filled squares) and known nuclei together with those nuclei that have been discovered at GSI (circles).

Studies of very neutron-deficient isotopes around ^{100}Sn lead to the discovery of a new island of alpha emission [SCH81], and to a systematic mapping of nuclear charge radii by collinear laser spectroscopy. Unexpectedly short half-lives were measured for very neutron-rich isotopes in the iron region, which is also of astrophysical interest [KLE86]. The discovery of the ground state proton decay, a new decay mode, showed that the border of nuclear stability had been crossed at its neutron-deficient side [HOF82]. The investigation of heavy elements was successful to identify the three up to now heaviest elements and to find access to the purely shell-stabilized superheavy nuclei at the upper end of the periodic table [ARM85]. These discoveries were possible with new experimental methods, developed at the GSI on-line mass separator and the velocity filter SHIP [ANG86]. For short-lived nuclei at the very limits of stability separation in-flight by the velocity filter SHIP has been proven to be a powerful tool for their investigation.

At relativistic energies projectile fragmentation is an exceptionally well suited process for producing and separating very exotic nuclei due to their small phase-space volume. This was already indicated by the early BEVALAC work [SYM79, WES79], where the projectile fragments were detected by means of particle-identification techniques after magnetic separation from the projectiles. Meanwhile, this new tool has also been used successfully at GANIL and at MSU. The drip lines of nuclear binding have been established experimentally up to $Z=6$ for neutrons [GUI85, LAN85, POU86] and up to $Z=20$ for protons [LAN86], including the most neutron-deficient nucleus reached so far, $T_z=-3$ ^{22}Si [SAI87]. Nuclear gross properties, such as radii up to ^{11}Li [TAN85, TAN85a],masses up to ^{26}F [GIL86], and β-decay half-lives [MUR82, CUR86, DUF84, DUF86] have been determined. Most recently detailed data on β-delayed radiation [DUF86, SHE86, BOR86] have become available. Small beam intensities and beams of large emittances together with energies too low for efficient separation of heavy projectile fragments are the drawbacks of existing facilities.

First measurements at the projectile fragment separator will consist of determining Z,A distributions of secondary beams above calcium, where incomplete stripping of the ions represents a limit for GANIL experiments [GUE86]. In addition to the identification of new nuclei and determination of drip lines,these measurements are essential to optimize yield and separation purity for a selected nucleus.

As far as decay spectroscopy of very neutron-deficient nuclei between calcium and tin is concerned, one may try to search for the hitherto unobserved two-proton ra-

dioactivity, e.g. from ^{39}Ti, and for new cases of single-proton radioactivity. In order to determine the high-Z limit of the astrophysical rapid proton capture process [WAL84], mapping of the proton drip-line and half-life measurements beyond ^{56}Ni are of interest. Measuring β-delayed γ and proton emission of such neutron-deficient nuclei would yield the strength of Gamow-Teiler β-transitions and would thus allow to study the hindrance effect for fp-shell nuclei [SEK86] all the way to ^{100}Sn [KLE86] in a unique way: Due to the high Q-values available (e.g. 19 MeV for ^{31}Ar → ^{31}Cl), the energy-window restriction is considerably less severe than in today's experiments. While the half-lives of the allowed (and superallowed) β-emitters do not present any problem for recoil separation, yield and purity of the secondary beam of interest are crucial experimental parameters. Yields of approximately 1 atom/s may be sufficient for measuring half-life and some characteristic decay radiation, but considerably higher yields are necessary for performing decay spectroscopy of weak transitions.

Nuclear structure physics and the understanding of the nucleosynthesis in astrophysics are a motivation for decay spectroscopy of neutron-rich nuclei. In the calcium region and from the nickel region onwards to heavier nuclei, experimental data on half-lives and β-delayed neutron emission may improve our understanding of isotopic anomalies in meteorites [ZIE85] and of r-process abundances, respectively [BOS86, KRA86]. An example for the latter kind of impact of nuclear-structure data on astrophysics is the recently measured ^{130}Cd half-life of 195 ± 35 ms. Calculated r-process exposure times based on this result support a steady-state rather than a short-duration scenario of the r-process [KRA86]. Of special interest are here the closed-shell neutron-rich nuclei with 50, 82, and 126 neutrons [MAY85]. The region with N = 126 below lead, where only very few isotopes beyond the heaviest stable ones are known, can be studied by fragmentation of ^{208}Pb.

More difficult to access is the region of β-delayed fission of neutron-rich isotopes below ^{238}U. Here a comparison of experimental with calculated probabilities for β-delayed fission [THI83] could yield valuable information on the termination of the r-process.

Besides these investigations of decay modes, gross properties such as nuclear radii and moments can be determined for short-lived ground-states or isomers.This can be achieved by laser hyperfine-structure spectroscopy after stopping the secondary beams from the FRS in gas. Alternatively, interaction cross-sections (and thus matter radii) can be deduced from measuring the transmission through a target [TAN85] .

The magnetic system to separate projectile fragments can also be used as a conventional magnetic spectrometer. Particles produced in heavy ion collisions emitted into the acceptance angle may be momentum-analyzed by the magnetic spectrometer. Especially spectra of fast light particles such as protons and α-particles are of interest. The observation of hadrons at the various thresholds within the SIS-energy range becomes possible. Working with a target at the symmetry plane of the magnetic system allows to study nuclear reactions at zero degree with a high momentum resolution. Peripheral collisions with Q-values exceeding 10 MeV can be investigated, e.g., excitations of giant resonance modes in relativistic heavy ion collisions, multi-nucleon transfer reactions and fission reactions of intermediate mass nuclei. Detectors for particles emitted from the target in coincidence with the energy-analyzed projectiles may be installed in addition. This spectrometer mode offers an option complementary to the multi-detector devices planned for the target hall. The restriction of beam intensity at the intermediate focal planes and the small acceptance angle may be a minor limitation at relativistic energies.

2.1.2 Atomic Physics Experiments

At energies of several MeV/u complicated charge exchange processes dominate the atomic interaction of heavy ions with matter [ANH85]. Empirical stripping criteria, effective charge concepts and scaling rules obscure the interpretation of experimental data for partially stripped ions in terms of deviations from the first Born approximation (the dependence on the square of the ionic charge state). This situation is much clearer at relativistic energies, where most of the heavy projectiles are completely stripped or only few charge states are occupied. For example, the higher order Mott, Bloch and polarization correction terms [AHL80] to the relativistic stopping-power formula calculated by Bethe can be investigated experimentally at SIS energies. Besides the more conventional methods to measure the stopping power of relativistic ions, radioactive nuclei from the FRS allow to use the inverted Doppler-shift attenuation method, especially, when liquid and gaseous multi-atomic targets are studied [NEU69]. Data on energy loss and angular straggling for relativistic heavy ions have not been published. Recent measurements of charge state distributions for uranium at 437 and 962 MeV/u [GOU84] have shown that experiments with few-electron ions reduce the complexity and therefore contribute more to the basic understanding of the interaction of ions with matter.

Investigations of axial channeling phenomena would be new for heavy ions at SIS energies. Measurements for heavy ions at intermediate energies [AND87] showed strong influence of the impact parameter under channeling conditions on the charge-state distribution and the X-ray spectra due to radiative electron capture.

The interest in few-electron systems has been discussed extensively in ref. [BER80]. The spectroscopy of few-electron systems needs a preparation of beams in well-defined ionic charge states [MAR86]. These beams can be prepared by stripping in a target at the entrance of the FRS and by magnetic analysis in the first stages of the spectrometer. The excitation of the electromagnetic transitions is achieved in a second target at the symmetry plane of the magnetic system. Here the emitted radiation will be observed in coincidence with the charge-state analyzed ion. This analysis is achieved in the second half of the spectrometer. For the detection of X-rays, electrons and electromagnetic radiation in other energy ranges, existing spectrometers might be used. Moreover, atomic collision processes of few-electron systems are of special interest. Electron-capture and -loss cross-sections in one-electron systems have been calculated theoretically, but measurements for heavy systems are lacking. Resonance transfers and dielectronic recombination at high energies can be studied. These measurements will complement the proposed measurements at the ESR electron cooling device.

2.1.3 Applications of Relativistic Radioactive Beams in Other Fields of Science

Relativistic heavy-ion beams penetrating through matter are characterized by large ranges (> 10 cm), a sharp Bragg-peak and relatively small range straggling (< 1 mm). These properties make them especially well-suited for applications in materials research, biology and medicine. In particular, the use of radioactive β^+-decaying beams of high energy in combination with Positron-Emission-Tomography (PET) imaging techniques opens a wide field of applications.

For medical diagnostic studies β^+-decaying radioactive beams can be precisely implanted into specific small volumes of the body, offering very clean conditions for measuring metabolic or blood flow rates by subsequent dynamical recording of the injected activity as a function of position and time. For these medical applications, the radioactive-beam injection time should be short compared to the half-life, to avoid decay losses during injection and an unnecessary high radiation dose. β^+-activities of the order of 10 kBq are needed to reach the optimum localization precision, which

is limited to a few mm by the range of the positrons before annihilation. Secondary beam fluxes higher than those presently available from the BEVALAC (~ $10^5 cm^{-2} \cdot s^{-1}$ with a beam area of several cm^2) are required. The high intensities and the small phase-space of the secondary beam from the FRS offer unique possibilities for further development of the techniques pioneered in Berkeley. At the exit of the FRS clean secondary beams of, e.g., ^{19}Ne with intensities up to $5 \cdot 10^8$/s within an area of a few mm^2 at the focal plane are expected. The β^+-activity needed for high-resolution imaging could be injected during one single SIS pulse, which would reduce the radiation dose to a minimum. The small size of the beams would be ideally suited for medical diagnostic studies such as blood-flow mapping or heart-valve function tests.

In radiotherapy, relativistic heavy-ion beams are used because of their superior depth dose distribution as compared to all other types of radiations. This allows to expose the tumor region to a high dose while the normal tissue around it is maximally protected. In order to take full advantage of the precise dose distribution, the localization of the beam inside the target area has to be of the same precision. Using radioactive β^+-decaying beams, the stopping points of the β^+-particles can be monitored by coincident detection of the two annihilation quanta. This method has been successfully tested and applied to heavy-ion treatment at the BEVALAC in Berkeley, using secondary beams of ^{11}C, ^{13}N, ^{15}O, ^{17}F, and ^{19}Ne [LLA84].

For solid state physics, Moessbauer-spectroscopy and other applications secondary beams allow the preparation of samples into which specific radioactive ions have been implanted. The range straggling for relativistic ions in the order of millimeters allows a homogeneous implantation which might complement neutron activation techniques of bulk material. The PET-imaging techniques described above are, in addition to their applications in medical science, a valuable non-destructive method for materials research.

2.2 Experiments with the Fragment Separator and the Storage Ring

The possibility to inject the separated and highly stripped radioactive beams into the ESR [FRA86] offers a new field of experiments. On the one hand it allows to experiment directly with stored and, if necessary, stochastically and electronically cooled ions of high phase-space density. For instance, ground-state properties, nuclear decays , hyperfine interactions of highly stripped ions or nuclear reactions can

be studied. On the other hand the ESR can be used to decelerate the stored ions and to provide low-energy radioactive beams.

As one of the most important ground state properties the mass of exotic nuclei circulating in the ESR can be measured. Masses of stable nuclei and neighbouring isotopes are known to a very high precision, while masses of exotic nuclei are usually determined via Q-value measurements with much lower accuracy. Many nuclear structure effects (e. g. shell closures, new regions of nuclear deformation, pairing energies etc.) were discovered in the past by direct mass measurements. These experiments were mainly done with on-line separators,using conventional ion sources. Their limitations due to nuclear life-times are circumvented by a new generation of experimental facilities in this field: the energy-loss spectrometer SPEG [GIL86] at GANIL and the time-of-flight spectrometer TOFI [VIE86] at Los Alamos. Both experiments are limited, however, to light nuclei.

The "tandem" FRS and ESR will be a unique tool for direct mass measurements of exotic nuclei up to Z = 92. Two complementary methods are proposed (see table 4.1): Operating the ESR in an isochroneous mode means that the time-of- flight through the optical elements is only dependent on the charge- over-mass ratio,but independent of the velocity [WOL86].As an additional advantage the particles pass repeatedly through the ESR (multiturn operation) to increase the accuracy. At present calculations show a stable multiturn operation for about 10 turns, but this is not a principal limitation. The other method ,which is suitable for high precision mass measurements with resolutions of about 1 MeV/c^2even for the isotopes above mass 100, needs the cooling facilities in the ESR. The momentum spread of the fragments after cooling will finally determine the mass resolution. The masses are then deduced from measurements of the revolution frequencies of the cooled ions (Schottky scan) [FRA86].

The hyperfine structure of stable and radiactive ions with few electrons can be studied with laser techniques in order to deduce radii and moments [HUB84].

The influence of the electron density and the hyperfine fields on nuclear decays of highly ionized ions can be investigated for the first time. One of these processes is the β-decay into discrete electron states which must have played a key role in nucleosynthesis [TAK86] . The strong hyperfine fields of unpaired inner electrons can influence nuclear half-lives via level mixing, e.g. the case of $^{104}In^{m}$[LYO66].

Nuclear structure studies in inelastic collisions can be performed in inverse kinematics. The accumulated exotic nuclei of high phase density colliding with the internal light targets (^{1}H,^{4}He,^{2}H,^{3}He) allow detailed studies of nuclear structure. Measuring the angle and the energy of the light recoil nuclei, the Q-values can be determined with a high resolution [BOS86a].

The cooled radioactive beam can be slowed down to the Coulomb barrier, allowing then in principle all the "UNILAC experiments" to be performed with exotic projectiles. This slowing-down method obviously avoids losses and contaminations due to secondary nuclear fragmentations which occur if degraders are used. On the other hand, the cooling-time in the storage ring requires a minimum life-time of the fragments of the order of 1 s. The deceleration down to the Coulomb barrier needs in addition roughly 2 s. At several MeV/u, the slowed-down radioactive beam is well-suited for experiments in solid state physics, because the unwanted surface effects observed in low energy (keV) implantations are completely avoided.

3. Fundamental Properties of Projectile Fragments

Heavy fragments in relativistic heavy-ion reactions result mainly from peripheral collisions. It has been observed experimentally that their projectile-like fragments move with almost the velocity of the beam and receive very little transverse momentum in the reaction, so that they are emitted close to 0^o in the laboratory system [HUF85]. Together with the observation that processes with at least one heavy fragment in the exit channel comprise about 2/3 of the (geometric) reaction cross section these kinematic properties make projectile fragments an ideal source of secondary exotic beams.

For quantitative predictions of secondary beam intensities the formation cross sections of individual isotopes in relativistic heavy-ion collisions have to be known. Subsection 3.1 comprises empirical expressions for these cross sections together with total nuclear and electromagnetic-dissociation cross sections which govern the absorption in various layers of matter in the FRS. The kinematic properties which follow from the fragmentation reaction mechanism are discussed in subsection 3.2. Finally, subsection 3.3 comprises the pertinent equations for the slowing-down of relativistic fragments in matter which have a major influence on both the kinematics and the resolution in A and Z of the FRS.

3.1 Cross Sections

3.1.1 Total Nuclear and Electromagnetic-Dissociation Cross Sections

At SIS energies the total nuclear cross section σ_n is mainly determined by the geometric dimensions of the colliding nuclei. We adopt here the parametrization by Kox et al. [KOX85]

$$\sigma_n = \pi r_o^2 (1 - \frac{B}{E_{cm}})(A_p^{1/3} + A_t^{1/3} + a\frac{A_p^{1/3} A_t^{1/3}}{A_p^{1/3} + A_t^{1/3}} - c)^2 \qquad (1)$$

with $r_o = 1.1$ fm and $a = 0.85$. The surface transparency parameter c is slightly energy dependent with a value of $c = 2.05$ at energies in the range E/A_p = 200-300 MeV/u and a value of $c = 1.9$ at higher energies. B is the usual expression for the Coulomb barrier.

In collisions of relativistic ions with large Z electromagnetic processes contribute appreciably to the total reaction cross section. These can be understood as an

excitation of the Giant Dipole Resonance (GDR) by the virtual photon spectrum generated by the target nucleus. The GDR then decays primarily into the 1n-, 2n- and f-channels. The total cross section for electromagnetic dissociation (ED) can be calculated easily by folding the Weizsäcker-Williams virtual photon spectrum [OLS81] with the tabulated Lorentz-curve parameters of the GDR [BER75]. The cross section for electromagnetic dissociation of U-projectiles on U is shown in Fig.3.1 for different energies in comparison with the geometric cross section. This demonstrates that for heavy ions like uranium ED processes cannot be neglected at energies around 1 GeV/u.

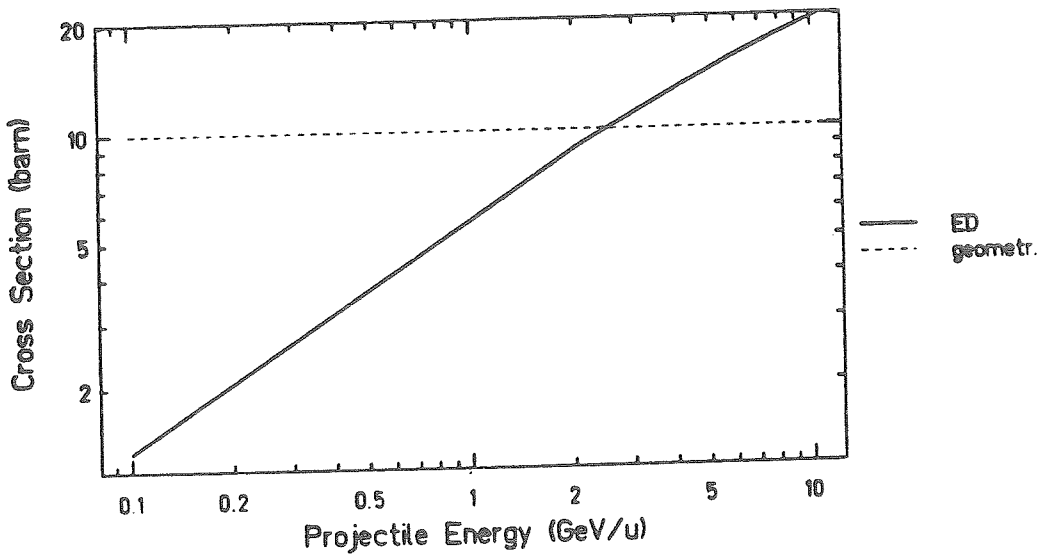

Fig. 3.1: Electromagnetic dissociation cross section for U+U as a function of the incident energy.

3.1.2 Production Cross Sections for Individual Isotopes

In the absence of reliable physical models for fragmentation processes the easiest and most reliable method to predict cross sections for the formation of individual isotopes is to parametrize measured A- and Z-distributions in terms of a few smoothly varying parameters. This approach has been introduced 20 years ago to parametrize the spallation cross sections measured in proton-induced reactions at various proton energies (see, e.g., [RUD66]). Systematic analyses (e.g. [CUM78],[POR79]) show that - at least in the case of light ions - the cross sections in heavy-ion induced reactions differ from those in proton-induced reactions only by the ratio of their geometric cross

sections. It has also been found that they become energy-independent above 3-10 GeV total kinetic energy. In the following we present modified formulae that give a satisfactory quantitative description of measured cross sections of specific *target fragments* for protons and heavy-ion projectiles at SIS energies. From symmetry reasons we can assume that the same formulae also describe the yield of projectile fragments. To obtain the corresponding projectile fragmentation cross sections, one has to interchange projectile and target in the following equations.

The cross section y(A,Z) for the production of a *target fragment* with mass A and charge Z (in the range $A_t/2 \leq A \leq A_t$) from the collision of a (light) projectile (A_p,Z_p) with a (heavy) target (A_t,Z_t) is written as:

$$y(Z,A) = Y(A) \cdot N_o(A) \cdot exp(-W(A)|Z - Z_{prob}|^U) \qquad (2)$$

with:

- $Y(A)$ = total cross section of all isobars with mass A
- $W(A)$ = width parameter of the charge distribution
- $Z_{prob}(A)$ = most probable charge at mass A
- U = 2 (Gaussian) for products more neutron-rich than Z_{prob}
  = 1.5 for products more proton-rich than Z_{prob}
- $N_o(A)$ = normalization factor to normalize the integral of the charge distribution to 1

For the *isobaric yield* Abul-Magd et al. [ABU86] have recently proposed the following expression:

$$Y(A) = \sigma_n P \cdot exp(-P(A_t - A)) \qquad (3)$$

where σ_n is the geometric reaction cross section and the slope constant P is given by

$$P = \frac{\epsilon}{E_o(\nu - 1)} \qquad (4)$$

where ϵ is the energy removed by each evaporated nucleon, E_o is the excitation energy transferred in each proton-nucleus collision, and ν is the average number of such collisions.

The parameters in eq.4 can be calculated in the framework of a simple physical model [ABU86]. For practical purposes it seems to be sufficient to parametrize P by the expression

$$P = exp(-7.57 \cdot 10^{-3} A_t - 2.584) \tag{5}$$

The second factor that determines the fragmentation cross sections is the exponential in eq.(2), the *charge dispersion*, characterized by the maximum $Z_{prob}(A)$, the width W(A), and the exponent U. It turns out that fragmentation products of any target close to the valley of β-stability can be described by the same charge dispersion. In this context, the valley of β-stability is parametrized approximately as

$$Z_t = \frac{A_t}{2.079 + 2.0486 \cdot 10^{-3} A_t} \tag{6}$$

The most probable charge, $Z_{prob}(A)$, and the width parameter W(A) have both been fitted with polynomials in A to the entire set of available experimental data. The distribution of isobars around $Z_{prob}(A)$ is also determined by the parameter U in the exponent of eq.(2). Rudstam [RUD66] has suggested an exponent of U = 1.5. We have found that the charge distributions are not symmetric around the maximum. Therefore we use a value of U = 1.5 only for the neutron-deficient side of the distribution, whereas a Gaussian (U = 2) fits the neutron-rich side.

With the parameters determined so far we can reproduce satisfactorily fragmentation cross sections for targets close to the valley of stability. For targets where the N/Z-ratio is different, however, it is found, at least for fragments close to the target, that the N/Z-ratio of the fragments reflects the N/Z-ratio of the target. With increasing mass loss from the target this "memory effect" goes to zero. Unfortunately there are no systematic studies of the shift of the yield distribution as a function of the displacement of the target from the stability line. Therefore in the present study an empirical shift of $Z_{prob}(A)$ has been introduced that reproduces the measured cross sections of $^{40}Ar + {}^{12}C$ and of $^{48}Ca + {}^{9}Be$ [VIY79, WES79].

To demonstrate the agreement with experiment that can be obtained by the parametrization described above, we present in Fig. 3.2 the charge dispersion of target fragments from p + Cu and Ar + Cu measured by Cumming et al. [CUM78]. The calculated cross sections for each nuclide have been divided by the mass yield Y(A) to give the fractional yield plotted in Fig.3.2 as a function of the distance of the fragment Z from the most probable one, $Z_{prob}(A)$.

As a specific example, we show in Fig.3.3 the region of nuclides predicted to be formed with cross sections between 10 mb and 1 nb by fragmentation of a neutron-deficient nucleus, ^{116}Sn, on a ^{12}C target. Table 3.1 lists a few examples of

Table 3.1: Estimated production rates of selected isotopes in projectile fragmentation reactions on a 1 g/cm² ^{12}C target

Beam	Intensity (1/s)	Nuclide	Cross section (nb)	Source Strength (1/s)
^{12}C	$5 \cdot 10^{11}$	^{8}He	35000[e]	$9 \cdot 10^{5}$
^{40}Ca	$5 \cdot 10^{11}$	^{33}Cl	27 mb	$7 \cdot 10^{8}$
		^{30}S	5 mb	$1 \cdot 10^{8}$
		^{30}Cl	16000	$4 \cdot 10^{5}$
		^{26}P	6000	$2 \cdot 10^{5}$
		^{20}Mg	2600	$7 \cdot 10^{4}$
		^{31}Ar	330	$8 \cdot 10^{3}$
^{48}Ca	$5 \cdot 10^{11}$	^{42}Ar	29 mb	$7 \cdot 10^{8}$
		^{44}Ar	8 mb	$2 \cdot 10^{8}$
		^{40}S	1.7 mb[e]	$4 \cdot 10^{7}$
		^{44}S	2000[e]	$5 \cdot 10^{4}$
		^{33}Na	30	$8 \cdot 10^{2}$
^{64}Zn	$5 \cdot 10^{11}$	^{60}Cu	44 mb	$1 \cdot 10^{9}$
		^{55}Co	20 mb	$5 \cdot 10^{8}$
		^{56}Cu	34000	$9 \cdot 10^{5}$
		^{47}Mn	1500	$4 \cdot 10^{4}$
^{76}Ge	$5 \cdot 10^{11}$	^{66}Ni	7 mb	$2 \cdot 10^{8}$
		^{68}Ni	1 mb	$3 \cdot 10^{7}$
		^{72}Ni	12000	$3 \cdot 10^{5}$
^{86}Kr	$5 \cdot 10^{11}$	^{44}S	5	$1 \cdot 10^{2}$
		^{76}Ni	4	$1 \cdot 10^{2}$
^{136}Xe	$5 \cdot 10^{11}$	^{130}Cd	200	$5 \cdot 10^{3}$
		^{120}Pd	4600	$1 \cdot 10^{5}$
		^{116}Ru	400	$1 \cdot 10^{4}$

[e] experimental value

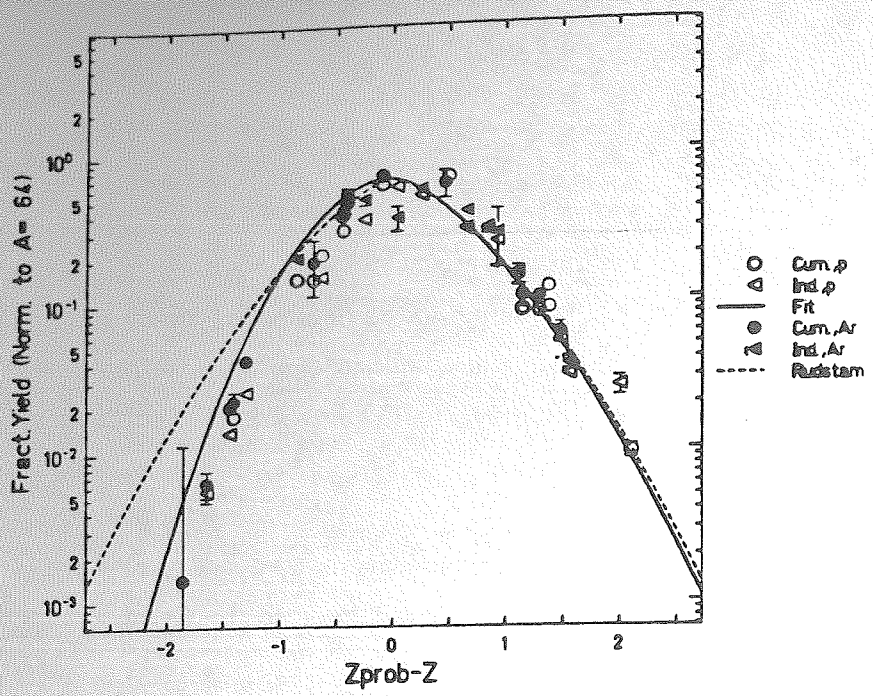

Fig. 3.2: Charge dispersion of fragments from the target fragmentation of Cu-nat with 12 GeV p and 8 GeV Ar in comparison with the predictions of eq.(2) (full line) and of [RUD66] (dashed line). The widths of the individual charge dispersion curves for each A have been normalized to A = 64.

predicted source strengths, calculated from the cross sections of eq.(2) with a target thickness of 1 g/cm^2 and the SIS beam intensities given in the table.

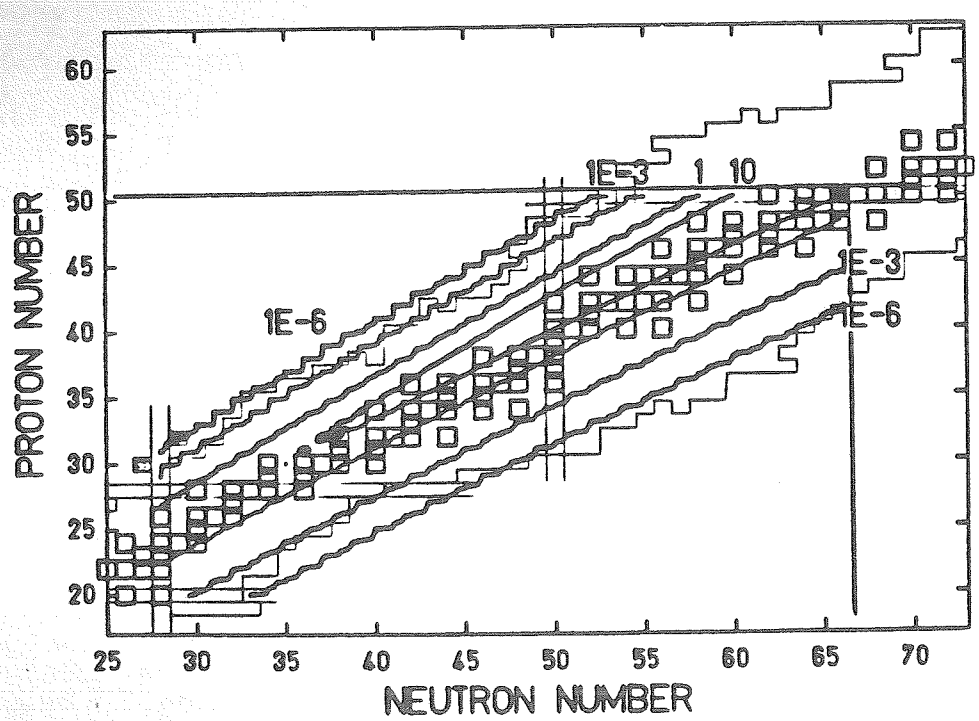

Fig. 3.3: Contour plot of the production cross sections (in mb) for ^{116}Sn fragments predicted on the basis of eq.(2). Contour lines are drawn between 10 mb and 1 nb. Squares indicate stable nuclei, the thin lines delineate the limits of known nuclei.

3.2 *Nuclear Reaction Kinematics*

The kinematic properties of the projectile fragments are of crucial importance for the performance of the FRS. One factor contributing to the final phase space distribution is the nuclear reaction. The momentum distributions of projectile fragments have been discussed in several review papers (e.g.[HUF85],[STO84]). They can be summarized as follows:

(i) The $p_{\|}$-distributions are to a good approximation Gaussians centered at $p_{\|} = p_o$ in the projectile frame. The width of the Gaussian can be related to the Fermi motion of the nucleons in the projectile spectator and is given by

$$\sigma(p_{\|}) = p_F \sqrt{1/5 \frac{A}{1 - A/A_p}} \tag{7}$$

with a Fermi momentum p_F = 221 MeV/c. For medium (A = 120) and heavy (A = 238) projectiles at kinetic energies of 1 GeV/u and for fragments with masses of $0.9 \cdot A_p$ this translates into a relative momentum width of 0.16% and 0.11%, respectively.

(ii) The mean velocity of fragments in the projectile frame is small and varies linearly with the excitation energy E^*, or, since $E^* = \varepsilon \Delta A$, with mass loss ΔA from the projectile. From fission fragment angular correlations, Kaufman et al. [KAU82] derive

$$\beta \cdot p_o = \epsilon \cdot \Delta A \tag{8}$$

with ε = 13 MeV; in the case of our examples in (i) with $\Delta A = 0.1 A_p$ we get p_o = 177 MeV/c and 355 MeV/c, respectively.

(iii) The variance of the transverse momentum is composed of the contribution from the intrinsic motion of the nucleons as in (i) and an additional contribution from the reaction of the order of $\sigma_n^2(p_\perp) \cong 0.3$ GeV/c [HUF85] so that

$$\sigma^2(p_\perp) = 3/2\sigma^2(p_{\|}) + \sigma_n^2(p_\perp) \tag{9}$$

For the same projectile fragments as above with masses $A = 0.9 A_p$ this gives deflection angles of on the order of

$$\theta = \sigma(p_\perp)/p_{\|} = 2.2...1.5 mrad \tag{10}$$

which are less than the design aperture of the FRS of ± 5 mrad.

From these considerations we conclude that only fragments close to the projectile ($0.8 \leq A/A_p \leq 1.0$) fit into the phase space transmitted through the FRS. This is visualized in Fig.3.4 which shows the variation of the angular spread of fragments with mass A from the fragmentation of 1 GeV/u ^{238}U projectiles in comparison with the angular acceptance of the FRS.

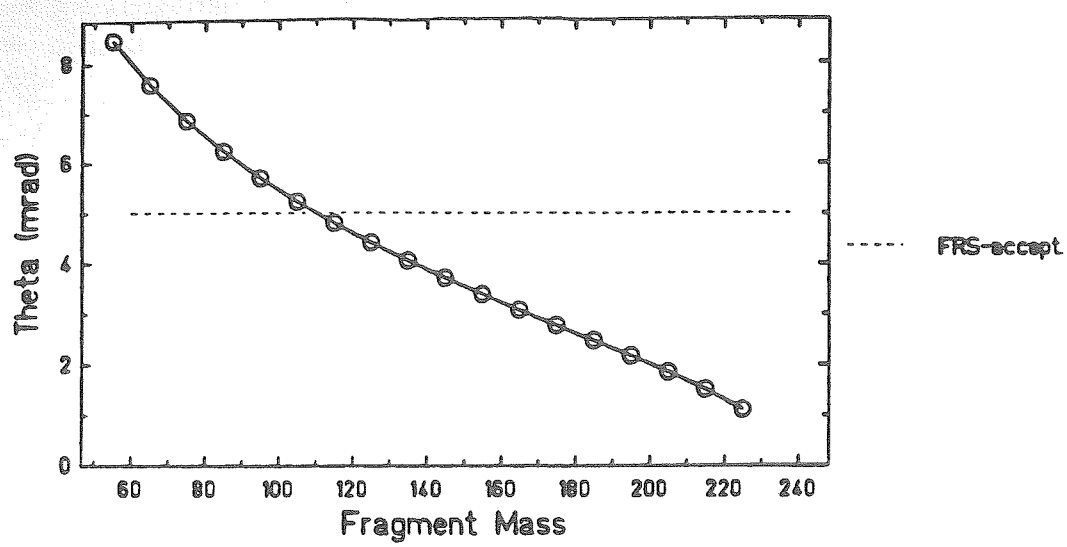

Fig. 3.4: Angular spread of fragments of 1 GeV/u ^{238}U projectiles.

Since at SIS also very fissile nuclei like uranium can be accelerated, one should consider in this context also the kinematic properties of projectile-fission fragments. Cross sections of individual fission products can be estimated with the help of tabulated fission yields for, e.g., 14 MeV-neutron induced fission [CRO77]. It turns out that the cross sections for these (neutron-rich) fission products are comparable to the yields of (neutron-deficient) spallation products. Their kinematic properties, however, are less favorable for separation in the FRS. Assuming symmetric fission into A = 100 fission fragments with 1 MeV/u in the moving frame, the momentum spread $\Delta p_{\|}/p_{\|}$ is 2.7% and consequently the deflection angle 27 mrad. These values are much larger than the acceptance of the FRS of ±5 mrad, leading to large transmission losses. Therefore we do not consider projectile-fission fragments an important source of neutron-rich radioactive beams.

3.3 Kinematics due to Slowing-Down in Matter

Another important contribution to the kinematics of projectile fragments comes from the slowing-down of the fragments in, e.g., the production target or in a degrader. For the production of radioactive beams target thicknesses in the order of 10% of the projectile ranges are used. Projectiles and fragments penetrating this rather thick layer have different energy losses. Fragments produced at different locations within the target therefore have in first order a square distribution in energy. The phase-space is further enlarged by fluctuations in energy loss and by angular straggling. Furthermore, a detailed knowledge of the charge exchange processes is essential to calculate the resolving power of the Bρ-Δp-method. In the following section we therefore want to summarize the formulae used to describe the stopping and charge exchange processes of relativistic fragments in matter.

3.3.1 Energy Loss and Range

Many theoretical aspects of the energy loss of relativistic heavy ions are presented in a review article by Ahlen [AHL80] and need therefore no detailed discussion here. Ahlen discussed the relativistic Bethe-formula and the incorporation of projectile-charge dependent correction terms.The Bethe stopping- power formula is based on first-order quantal treatment and depends therefore on the square of the projectile charge. Based on the Bethe formula stopping powers and ranges for heavy ions are often simply scaled from the corresponding values for protons at same velocity.Depending on the energy region this procedure is accurate to about 10-20%.

To separate neighbouring isotopes by their slowing-down characteristics requires a more precise knowledge of the stopping power, however. Therefore it is necessary to include higher-order corrections to the Bethe stopping- power formula: the Mott term (M) which accounts for the finite size of the charge distribution [AHL80], the two Bloch terms B_{nr} and B_r[AHL82] to describe properly the electron binding in close-collision events, the density effect (δ/2), the low-velocity Barkas effect (J) [JAC72], and the inner-shell corrections (C/Z_2) [AHL80]. These correction terms depend on up to the fifth power of the fragment charge Z_1. The resulting formula reads

$$\frac{dE}{dx} = \frac{4\pi N e^4 Z_1^2 Z_2}{m_e c^2 \beta^2}\left[\ln\frac{2m_e c^2\beta^2}{I(1-\beta^2)} - \beta^2 - \frac{C}{Z_2} - \frac{\delta}{2} + M - B_{nr} + B_r\right] J \qquad (11)$$

Z_1, Z_2 nuclear charge of the fragment and the stopping material

e, m_e charge and mass of the electron

$\beta \cdot c$ velocity of the fragment

N number of atoms per unit volume in the stopping material

I mean ionisation energy of the stopping material

At energies where the fragments are not fully ionized we use the effective charge concept of Brandt et al. [BRA82]. The nuclear stopping is only a very small contribution, nevertheless we have included the analytical expression deduced by Biersack et al. [ZIE85a].

From the stopping power, the mean integrated path length $R(E_i)$ for a fragment having the kinetic energy E_i is obtained as

$$R(E_i) = \int_0^{E_i} \frac{dE}{dE/dx(E)} \tag{12}$$

with dE/dx given by eq.(11). At relativistic energies, the integrated path lengths are practically identical to the projected ranges because the influences of angular deflections and deviations from the continous slowing-down model are negligible for heavy ions.

With the help of the range $R(E_i)$ calculated according to eqs.(11) and (12), one can also calculate the energy loss in a thick layer of matter as, e.g., the production target of the FRS. With d being the thickness of such a layer, the energy loss

$$\Delta E(d) = E_i - E_f \tag{13}$$

can easily be calculated from the residual ranges before and after the layer, $R(E_i)$ and $R(E_f)$, since

$$R(E_f) = R(E_i) - d \tag{14}$$

As mentioned above, the fragment energy distribution behind the target is mainly determined by the different locations within the target where the fragmentation occurs, since projectile and fragment have different energy loss in the target material. The resulting energy spread, which one could call 'location straggling', is illustrated in Fig.3.5 for different fragment atomic numbers Z_1 produced in the fragme ntation of 1 GeV/u uranium in a 1 g/cm^2 Be target. It is obvious that the energy spread is the more pronounced the more the atomic numbers of the projectile and the fragment differ.

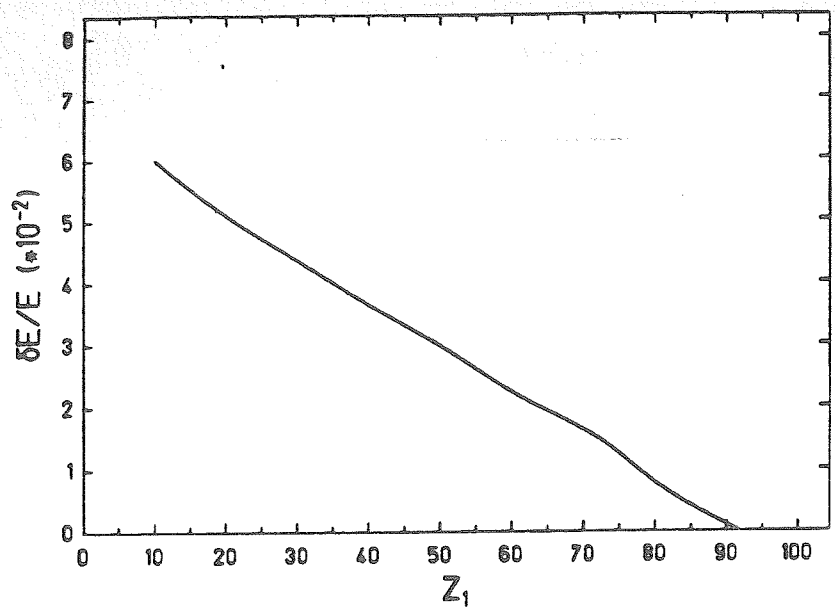

Fig. 3.5: Energy spread as a function of the fragment atomic number Z_1 for fragments near stability from the reaction of 1 GeV/u uranium ions impinging on a 1 g/cm^2 Be target. Only the energy spread is shown that is due to the different locations within the target where the fragment is produced.

3.3.2 Energy Straggling

As will be shown below the energy straggling at relativistic energies is small even for the relatively thick degraders used in the FRS. To calculate the energy straggling in thick degraders we have follwed the concept of Tschalär [TSC68] where the variation of the stopping power due to the significant changes in energy has been taken into account, i.e. the additional broadening due to the smaller energy loss of the higher-energy particles in the distribution is included in the calculation. The energy straggling is written as

$$\delta E^2 = \left[\frac{dE}{dx}(E_f)\right]^2 \int_{E_f}^{E_i} \frac{\sigma_E^2(E)}{\left[\frac{dE}{dx}(E)\right]^3} dE \qquad (15)$$

with $\sigma_E^2(E) = 4\pi e^4 Z_1^2 Z_2 (1-\beta^2/2)/(1-\beta^2)$ being the Bohr term for the energy straggling. E_i and E_f are the fragment energies before and behind the thick degrader, respectively. This description is expected to be valid only when the ions are fully stripped. In our application this condition is nearly always fulfilled.

In Fig.3.6 we present numerical results for the relative energy straggling δE/E of 1 GeV/u ^{212}Pb in Be as a function of the degrader thickness, neglecting the incident-energy spread discussed in subsection 3.3.1. The thickness is given in units

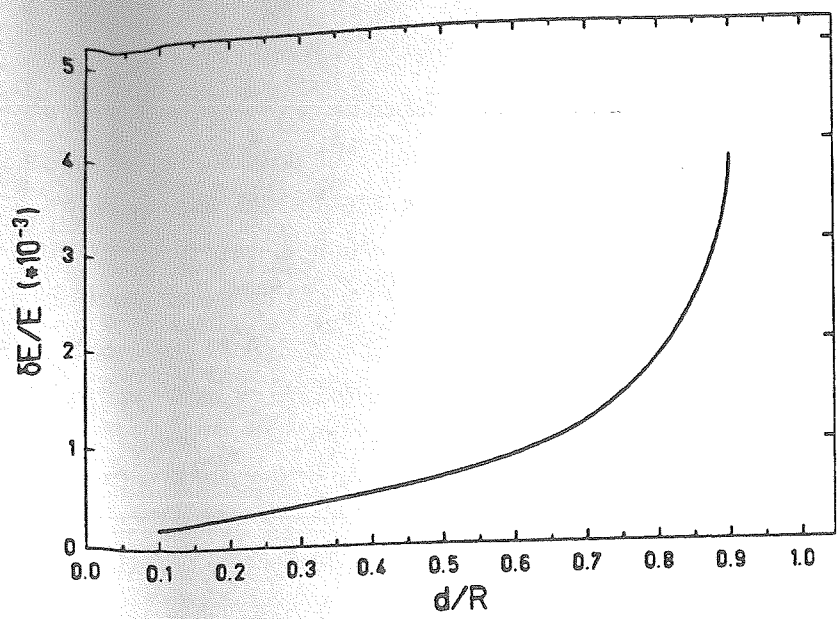

Fig. 3.6: Relative energy straggling of 1 GeV/u ^{212}Pb ions in a Be degrader as a function of the degrader thickness (given as fraction of the total range).

of the total range of ^{212}Pb ions in Be. Obviously the energy straggling is small compared to the large variation in energy induced by the 'location straggling' discussed above. The nucleus ^{212}Pb is chosen as an example because this fragment is used in the following sections to illustrate the separation characteristics of the FRS (see section 4).

3.3.3 Range Straggling

Using the same nomenclature as in eq.(15), the range straggling can be written as

$$\delta R^2 = \int_0^{E_i} \frac{\sigma_E^2(E)}{\left[\frac{dE}{dx}(E)\right]^3} dE \qquad (16)$$

Numerical calculations of the range straggling using eq.(16) yield only a few mg/cm^2, if again the incident-energy spread is neglected. This has to be compared with a target thickness of the order of g/cm^2 used to fully exhaust the momentum spread ($\Delta p/p = \pm 1\%$) transmitted through the FRS.

3.3.4 Angular Straggling

Multiple scattering of the projectiles and the fragments in the target or in the degrader gives rise to an enlargement of the phase-space resulting in transmission losses and introducing higher-order image aberrations. The angular distribution of the fragments is a convolution of the contributions due to the nuclear reaction, the multiple scattering in matter and the emittance of the incident projectile beam. To first order these contributions are uncorrelated and add quadratically. Ion optical focussing is therefore done in a way that the target and the degrader are put in positions where the phase-space ellipsoid is upright (waist). This procedure minimizes the deterioration of the phase-space due to the insertion of matter into the path of the fragments.

Experimental data on multiple scattering of heavy ions at low energies agree well with the nonrelativistic theory of Sigmund and Winterbon [SIG74]. For relativstic ions Nigam et al. [NIG59] and Marion and Zimmerman [MAR67] extended the theory of Moliere [MOL48]. Since no experimental data for relativistic heavy ions are published, however, it is adequate to use a much simpler formula [PAR84] to estimate the multiple scattering of the relativistic reaction products:

$$\sigma(\alpha) = \frac{14.1 MeV/c}{p\beta} Z_1 \sqrt{d/L_r} \left[1 + \frac{1}{9} \log d/L_r\right] (radian) \qquad (17)$$

The formula gives the standard deviation of the straggling angle for a degrader of thickness d measured in units of the radiation length, L_r. P is the momentum and β the ion velocity. As an example Fig.3.7 shows the variation of $\alpha_{1/2}$ as a function of target thickness (again given as fraction of the total range) calculated according to eq.(17) in comparison with the angular spread introduced by the emittance of the SIS beam and by the fragmentation reaction mechanism (see subsection 3.2).

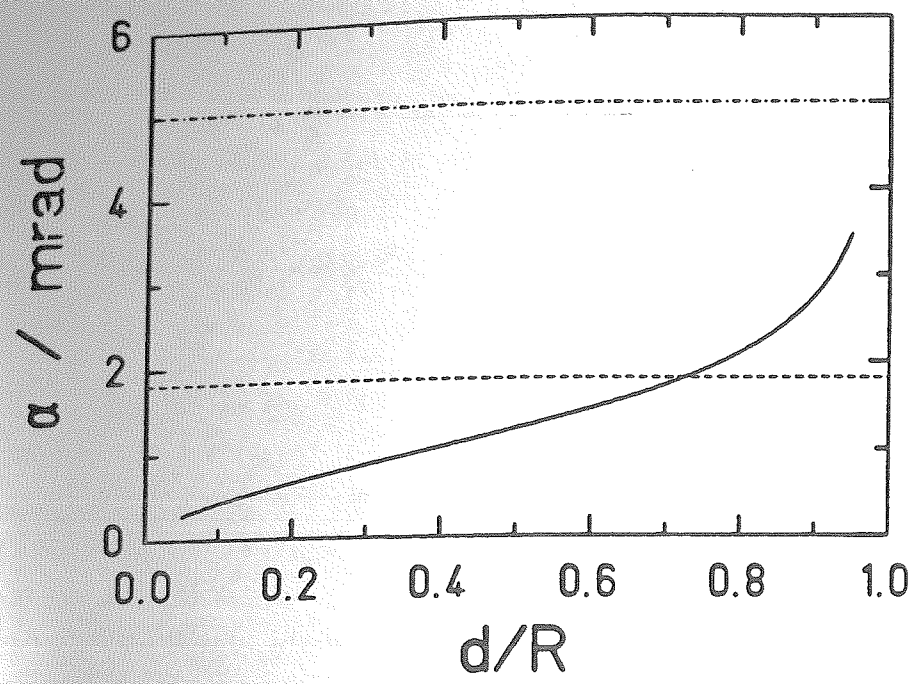

Fig. 3.7: Angular straggling (full line) for 1 GeV/u ^{212}Pb fragments in a Be degrader as a function of the degrader thickness. The contributions from the nuclear reaction (dashed line; fragmentation of 1 GeV/u ^{238}U) and from the emittance of the SIS beam are indicated separately (dashed-dotted line) .

3.3.5 Charge Distributions at Relativistic Energies

Charge-exchange processes determine the kinematics of the projectile fragments in so far as the incident energy must be selected high enough that most of the fragments are fully ionized. Different charge states of the fragments are deflected differently in the magnetic dipole sections of the FRS and cause ambiguities in the fragment A and Z identification.

In general the cross sections for loss and capture of electrons are difficult to calculate especially when multiple excitations and charge transfers are dominating processes [ANH85,BET76]. Here we need to consider only charge exchange processes of hydrogen-like fragments, however. Furthermore, target and degrader are thick enough to reach charge state equilibrium. Therefore the ratio of the number of fully stripped fragments (n_0) and of fragments with one electron (n_1) is directly given by the ratio of the electron loss (σ_l) and electron capture (σ_c) cross sections:

$$n_o/n_1 = \sigma_l/\sigma_c \tag{18}$$

The capture cross section is the sum of the cross sections for radiative electron capture, σ_{REC}, given by Gould et al. [GOU84], and the relativistic cross section for nonradiative capture as calculated by Brinkmann and Kramers [BRI30]. For the former we have

$$\sigma_{REC} = \frac{\left[(\gamma-1)+\frac{B_n}{m_e c^2}\right]^2 X\sigma_o}{\gamma^2-1} \tag{19}$$

where B_n is the binding energy of the electron in the n^{th} shell, X is the fraction of the shell which is empty, and σ_φ is the photoionization cross section; β and γ are the usual relativistic velocity factors. The nonradiative capture contribution is small at relativistic energies. The cross section for ionizing a K-shell electron can be derived from Bethe's stopping theory:

$$\sigma_l = 4\pi a_o^2\left(\frac{\alpha}{\beta}\right)^2\frac{1}{B_k}(Z_1^2+Z_2)f_k\left[\ln\frac{(2\beta\gamma/\alpha)^2}{0.048B_k}-\beta^2\right] \tag{20}$$

where a_o is the Bohr radius of hydrogen, α the fine-structure constant, and B_K the binding energy of a K-shell electron. The factor f_K is proportional to the transition strength from the K-shell to the continuum and has a numerical value of of 0.29 for the ionization of U^{91+} [GOU84].

With the equations given above we have calculated the energies for the ratios $n_1/n_o = 1$ and $n_1/n_o = 0.1$ as a function of the fragment charge, Z, for a Be degrader. The resulting curves are plotted in Fig.3.8.

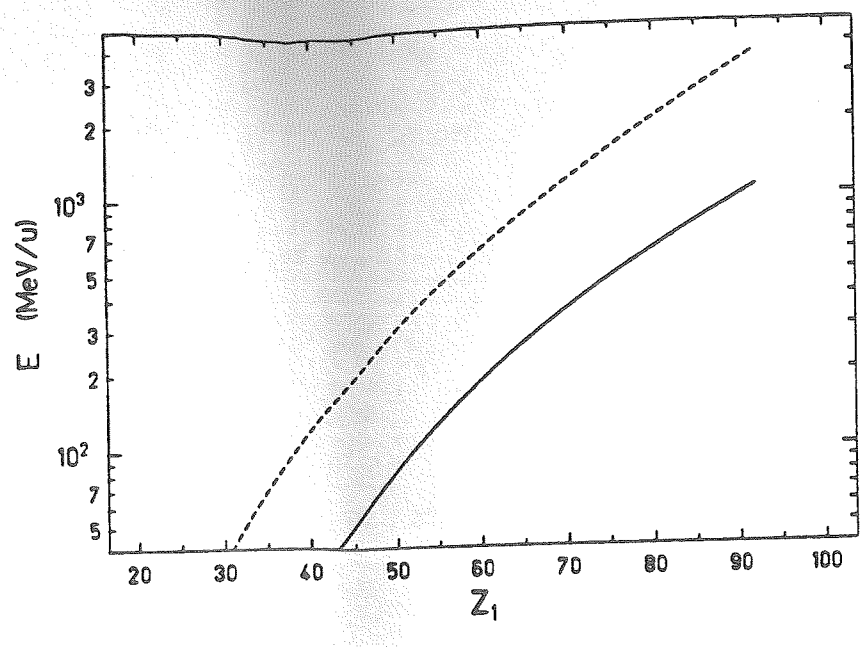

Fig. 3.8: Energies where 50% (thick line) and 90% (dashed line) of the fragments with atomic number Z_1 are fully stripped when penetrating a Be degrader that is thick enough to ensure charge state equilibrium.

They allow to select the energy range for an efficient operation of the FRS. Other constraints for the useful energy ranges are dicussed in more detail in sect.4.

4. Separation of Projectile Fragments

4.1 Selection of the Separator Type

The requirements for the planned projectile fragment separator are:

a. Acceptance of all projectiles and intensities, emitted by the 18 Tm synchrotron SIS

b. Separation of projectile fragments in A and Z with low contaminations of unwanted nuclides.

c. High production rates and transmission for radioactive beams.

d. Injection of the separated particle beam into the ESR without significant losses.

The specifications of the SIS, ESR and the requirements for the separator are given in table 4.1.

Conventional ion-optical devices principally can only separate in A/Z, consequently a figure for the resolution required for an isotopical separation is difficult to estimate, even more as we generally deal with fully stripped ions. This difficulty is illustrated by the example of the separation of ^{100}Sn , this beam can be contaminated with all elements A/Z = 2. Only a separator with a resolution of more than 10^4 could separate all neighbouring nuclides using the A/Z difference caused by the mass defect. Generally we consider a resolution of 10^3 to be feasible for beams with properties as listed in table 4.1.

In principle, a crude A/Z-identification is possible with a single dipole magnet. The first-order resolution of a dipole magnet is determined by the source emittance $2x_0 2x'$ and the area S covered by the beam in the bending plane of the magnet [BRO70, WOL71]:

$$R_{B\rho} = \frac{B \cdot S}{2x_0 2x'_0 B\rho} = \frac{b \cdot \theta}{2x_0 2x'_0} \qquad (21)$$

where Θ denotes the angle of deflection, b the averaged beam width in the dipole, and $B\rho$ the magnetic rigidity of the beam. With dipole magnets allowing a beam width of 10 cm and a bending angle of 60^{o}, a resolution $R_{B\rho} = 1300$ is achieved for the given emittance of 20 π mm mrad. The A/Z-resolution is given by:

$$R_{A/Z} = \frac{1}{\gamma^2 \frac{\Delta v}{v} + \frac{1}{R_{B\rho}}} \qquad (22)$$

$\Delta v/v$ denotes the relative velocity spread of the fragments. As the reaction products emerge from a target with a velocity spread in the order of 1%, the resolution is limited to 50 - 100, dependent predominantly on the energy spread in the target.

Using time-of-flight or Cerenkov detectors, the particle velocity can be measured event-by-event. Then $\Delta v/v$ in eq. (22) is given by the velocity resolution of the setup. Therefore the TOF-$B\rho$ method provides sufficient resolution, but it is limited to small counting rates and does not fulfill the condition of spatial separation necessary for injection into the ESR.

The possibility to use an rf cavity with a transversal electric field has been discussed by Hinderer [HIN85]. The particles passing the cavity close to 0^{o}-phase are deflected according to the rf phase passing the cavity. As a minimum requirement for separation, bunches of particles with velocities to be discriminated have to enter the condenser separated in time. The separation along the flight path is:

$$r_v = \frac{l}{\beta \cdot c \cdot \Delta t} \qquad (23)$$

where l is the distance between target and cavity and Δt the bunch width of SIS. For a practicable flight path in the order of 10 m and $\beta = 0.3$, the SIS bunch width must be below 100 ps to obtain a resolution of 10^3. Similar considerations hold for the combination of a rf buncher with longitudinal electric field to compress the velocity spread of the projectile fragments for a separation in dipole magnets with high resolution (eq. 22), proposed by B. Franzke [FRA85].

We have also investigated the separator with electrostatic and magnetic field, the classical Mattauch-Herzog type. In analogy to the magnectic field the resolution of the electric deflection condenser can be written as [WOL73]:

SIS parameters for maximum beam intensity

beam rigidity.		18	Tm
energy, max. for U^{92+}		1.4	GeV/u
ions available		Ne to U	
emittance	x x′	20 π	mm mrad
	y y′	10 π	mm mrad
time structure	macro (repetition rate)	1 to 3	1/s
	micro (bunch width)	40	ns

ESR parameters for maximum beam intensity

beam rigidity		10	Tm
Energy range (output)		3-500	MeV/u
acceptance	x x′	20 π	mm mrad
	y y′	10 π	mm mrad
momentum width after cooling	Δp/p	$< 10^{-5}$	
cooling time		0.1-1	sec

Parameters of the fragment separator

solid angle	< 0.42	msr
momentum width	2 %	
beam rigidity, maximum	18	Tm
energy range	0.1-1.4	GeV/u
output momentum width (spec. mode)	10^{-3}	
average target thickness (Al)	1	g/cm^2
transmission (approx.)	60 %	

Table 4.1: Parameters for SIS, ESR and the projectile fragment separator

$$R_{F\rho} = \frac{F \cdot S}{2x_3 2x_0' F\rho} = \frac{(U^+ + U^-) \cdot L}{2x_0 2x_0' F\rho} \qquad (24)$$

with F denoting the electric field strength and Fρ the electric beam rigidity, L the condenser length, U^+ and U^- the voltages applied to the condenser plates. For the combination of an electric and a magnetic field the obtainable resolution in A/Z is

$$R_{A/Z} = R_{F\rho}/\gamma^2 \qquad (25)$$

The calculated resolution for 0.5 GeV/u particles in a 1 MV condenser of 20 m length is of the order of 50 and decreases to 10 for 1 GeV/u particles.

Gas-filled systems used with great success for the separation of fission fragments [ARM71] obviously cannot be used for almost fully stripped ions in the energy range above 0.1 GeV/u.

The most promising approach to achieve isotopic separation of relativistic heavy ions is the combination of magnetic separation and energy loss in a degrader, a technique already used at CERN [LAN58] and Argonne [MAR62] for the separation of K-mesons, and recently refined and applied with great success for heavy ions at GANIL with the LISE separator [DUF86]. A separator of this type consists of an achromatic magnetic analyzer with a degrader, located at the intermediate focus in the dispersive plane. In the first part of the separator, the magnetic sector field generates a crude A/Z separation. Nuclei with similar A/Z pass the degrader and are dispersed according to their different final magnetic rigidities in the second stage. With an appropriate shaping of the absorber, an isotopic separation is possible even for fragments with a considerable momentum spread.

A comprehensive comparison of the different separation methods is given in table 4.2.

Table 4.2: Comparison of Various Ion Optical Methods of Isotope Separation

Method	Separation-Parameter	Resolution in	Limit	Limitations	ESR-Storage of separated beam	Comments
mag. Dipole 30°	$B\rho$	A/q	100	$\frac{\Delta v}{v}$, reaction kinematics	yes	For pre-separation
mag. Dipole 30° + TOF	$B\rho$, TOF	A/q	500	TOF-Resolution	no	Rate < 10^6, additional measurement combined with other separation
mag. Dipole 30° + Cerencov	$B\rho$, β	A/q	10^4	$\beta > 0.8$	no	"
mag. Dipole + longitudinal RF	$B\rho$, $\Delta v << \Delta v_0$	A/q	10	SIS-micro-pulse	yes	Compression of $\frac{\Delta v}{v}$, usable if SIS-pulse width < 0.5 ns
mag. Dipole + transversal RF	$B\rho$, TOF	A/q	10	SIS-micro-pulse	yes	Particle bunches pass at 0°, harmonics
Recoil-Mass-Separator	$B\rho$, $F\rho$	A/q	50	Electric field	yes	High-voltage condenser, 20 m length, 1 MV
Gas-filled magnets				$E/A \lesssim 0.1$ GeV/u	yes	
Achromat (2 x 60°) + absorber	$B\rho$, ΔE	Z A	100 200	$B\rho$-Resolution of Separator	yes	Also $\frac{\Delta v}{v}$ compression mode possible
Separator + ESR, "TOFI" mode	$B\rho$, TOF		10^3 - 10^4	beam stability in ESR		ESR operated in isochronous mode
Separator + ESR	$B\rho$, $\frac{\Delta v}{v} < 10^{-5}$		10^5 - 10^6	electron cooling		

4.2 The Momentum-Loss Achromat

In this section, the characteristics of the momentum-loss achromat which we propose to be constructed for the isotope separation of projectile fragments will be discussed. A detailed study of the momentum-loss achromat can be found in ref. [SCH87].

4.2.1 General Description

The momentum-loss achromat which is schematically presented in fig. 4.1, separates an individual isotope by combining two different selection criteria. As an example, the corresponding selection lines on the chart of nuclei are demonstrated for the separation of ^{212}Pb in fig. 4.2. These selection lines correspond to nuclei which are deflected to the same positions in the intermediate focal plane and at the exit of the separator, respectively.

In detail, the fragments are separated in the following way: The beam hits the production target with a thickness in the order of 10% of the projectile range. In the focal plane after the first dipole a magnetic selection according to the momentum-

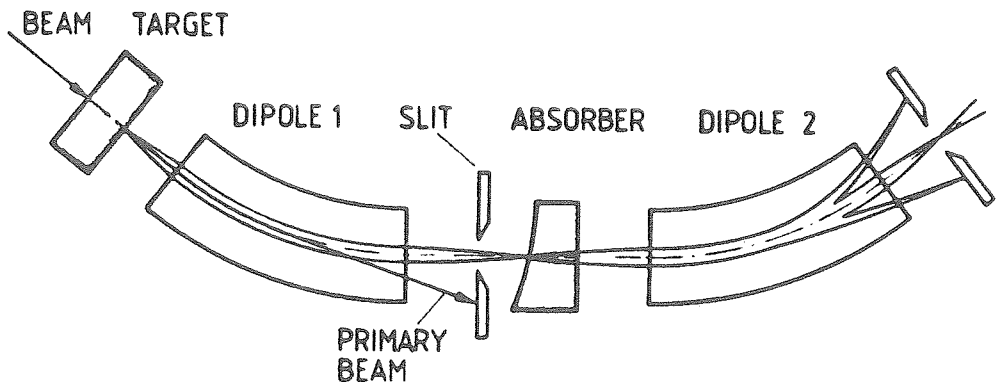

Fig. 4.1: Schematic drawing of the momentum-loss achromat. The first section separates the projectile fragments according to their initial magnetic rigidity. The deflection at the exit of the system is proportional to the momentum-loss ratio p_{z2}/p_{z1} in the intermediate degrader. The profile of the degrader preserves the achromaticity of the system which is essential for a good resolution, independent of the initial momentum width.

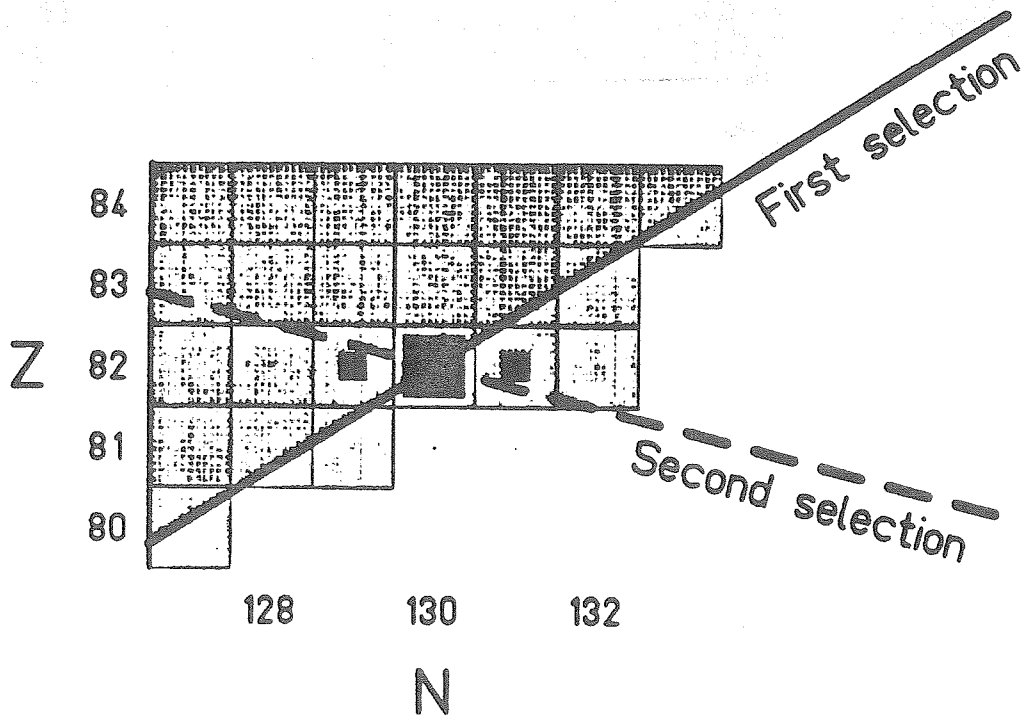

Fig. 4.2: Selection lines and transmission values of the momentum-loss achromat on a chart of nuclei. The system is tuned to select ^{212}Pb, produced by a beam of ^{238}U in a 0.5 g/cm^2 Be target. An intermediate degrader of 5.3 g/cm^2 Pb is used. The resolution of both magnetic sections is $B\rho/\Delta B\rho = 1500$.

over-charge ratio is made. Even if the velocity distribution of each isotope is narrow, this separation cannot select a single isotope, but a variety of nuclei with $A/Z \approx$ const still reaches the intermediate degrader. The electronic momentum loss in this thick degrader (in the order of 50% of the range of the fragments) depends on the parameters (A, Z and v) of the fragments in a different way compared to the magnetic deflection in the first stage. This is the key for the possibility of separating single isotopes. In a second magnetic dipole section the products are deflected according to their residual magnetic rigidity. Dependent on the magnetic rigidity of the ions in the first stage, the profile of the degrader can be chosen in a way that the momentum dispersion of a selected fragment is compensated by the second dipole section, that means the system is achromatic. This is the operation mode of the momentum-loss achromat. In a magnetic system which is achromatic without inserting an energy degrader, like the LISE spectrometer at GANIL [ANN86], the achromaticity is preserved if the ions loose a fixed portion of their momentum in the intermediate degrader.

The slope of the second selection line on the chart of nuclei and the quantitative determination of the transmission of the individual isotopes as given in fig. 4.1 are the result of a numerical calculation. For this calculation, the development of new ion-optical methods was necessary. These methods and the investigation of the general features of the Bρ-Δp selection are presented in the following sections.

The separation of the isotope ^{212}Pb will be repeatedly discussed as a difficult test case. For this heavy isotope, a high resolving power of the system is necessary. Additionally, the large mass difference to the nearest available projectile ^{238}U complicates the separation.

4.2.2 Methods for Studying the Properties of the Momentum-Loss Achromat

4.2.2.1 Extended ion-optical treatment of multidimensional distributions

In order to predict the separation characteristics of the momentum-loss achromat, ion-optical calculations have to incorporate all fluctuations of the relevant parameters of the ions passing through. Therefore, the transmission of individual isotopes was calculated with a computer program which handles additionally to the ion-optical imaging the convolution of all relevant effects which broaden the phase-space distributions. This program is especially well suited to determine the general properties as the separation characteristics or the optimum operation parameters of the separator.

The distribution of the projectiles at the target position is assumed to be Gaussian in momentum, angle and position. The momentum spread of the fragments due to the reaction is included according to the fragmentation model of ref. [GOL74]. The momentum-loss differences in the target have to be considered for projectiles before and for fragments after nuclear reactions. This gives rise to a rectangular-like momentum broadening of the fragments at the exit of the target. Gaussian-like broadenings due to energy straggling and angular straggling of projectile and fragment in the target are included, too.

The deflection behind the first dipole section is calculated according to the magnetic rigidity of the particles, and the size of the image in the intermediate focal plane is determined by the size of the beam spot at the target times the magnification of the

first section. The influence of the higher-order aberrations of the first dipole section is incorporated by folding the image size with the gaussian distribution which corresponds to the image of a point. The energy loss of the ions in the profiled degrader is calculated at each position. The shape of the degrader is determined exactly to meet the achromaticity condition of the system. This is essential for optimizing the resolving power. As in the target, gaussian-like broadenings due to energy straggling and angular straggling are included.

The dispersion and the influence of higher-order aberrations in the second section are calculated in the same way as in the first one. Finally the range distribution of the fragments in a stopping medium at the exit of the momentum-loss achromat is determined.

The transmission of the device is calculated for all projectile fragments by imposing several windows, e.g. slits in the intermediate focal plane and at the exit of the system as well as a range selection by using a thin catcher foil at the exit of the system. Moreover, limitations in the angular acceptance of the instrument are considered.

In addition, charge-exchange processes and secondary nuclear reactions of the fragments during their passage through matter are taken into account.

4.2.2.2 Extended first-order ion-optical treatment in the matrix formalism

In the following section we will show, how the first-order ion-optical treatment of the magnetic separation combined with the energy loss in a degrader can be formulated in the matrix description.

The parameters conventionally used to describe the trajectory of a charged particle through an ion-optical beam line are position x, angle x', ionic charge q, and momentum p. For the calculation of a spectrometer to provide isotopic separation, we need a notation which also includes the rest mass m and the nuclear charge Z. Consequently, the following formulae are written for fully stripped ions, a condition, which generally can be met for relativistic heavy ions. For convenience of the relativistic calculations we introduce the relativistic velocity parameter v :

$$\nu = \beta \cdot \gamma \quad with \quad \beta = v/c \quad and \quad \gamma = (\sqrt{1-\beta^2})^{-1} \tag{26}$$

All quantities refer to a central trajectory and to reference particles with the average charge, mass, and velocity which scale in relative units (the reference quantities are denoted by a ^ sign) :

$$\delta Z = \Delta Z/\hat{Z}, \quad \delta m = \Delta m/\hat{m}, \quad \delta \nu = \Delta \nu/\hat{\nu} \tag{27}$$

In the first-order approximation the equation of motion is expanded in a Taylor series. For the position coordinate, for instance, we obtain:

$$x = \frac{\partial x}{\partial x_0} x_0 + \frac{\partial x}{\partial x_0'} x_0' + Z_0 \frac{\partial x}{\partial Z_0} \delta Z_0 + m_0 \frac{\partial x}{\partial m_0} \delta m_0 \quad \ldots \quad + \nu_0 \frac{\partial x}{\partial \nu_0} \delta \nu_0 \tag{28}$$

The motion of the particle can be described by a set of equations written in matrix form [PEN61,BRO70]. In our coordinates defined above the transfer matrix for a dispersive magnetic separator stage with point-to-point imaging is:

$$\begin{bmatrix} x \\ x' \\ \delta Z \\ \delta m \\ \delta \nu \end{bmatrix} = \begin{bmatrix} V & 0 & D_Z & D_m & D_\nu \\ V' & 1/V & D_Z' & D_m' & D_\nu' \\ 0 & 0 & 1 & 0 & 0 \\ 0 & 0 & 0 & 1 & 0 \\ 0 & 0 & 0 & 0 & 1 \end{bmatrix} \cdot \begin{bmatrix} x_0 \\ x_0' \\ \delta Z_0 \\ \delta m_0 \\ \delta \nu_0 \end{bmatrix} \tag{29}$$

The first element in the first line, V, denotes the magnification. The second element of the first line is zero, as at the focus the coordinate is independent of the initial angle x'_0. The dispersion coefficients D_Z, D_m, and D_ν stand for the dispersions in charge-, mass-, and velocity-parameter ν, respectively. The corresponding coefficients, denoted by a prime, refer to the angular dispersions. As the conservation of

phase space requires that the determinant of the beam transformation matrix is unity, the angular magnification is 1/V for this special case.

The magnetic rigidity is given by

$$B\rho = \frac{m \cdot c \cdot \nu}{Z} \tag{30}$$

and therefore the dispersion coefficients are related by:

$$D_\nu = D_m = -D_Z = D \tag{31}$$

D denotes the dispersion coefficient in the common (momentum) notation [BRO70].

The coordinate transformation by the degrader can be written as:

$$\begin{bmatrix} x \\ x' \\ \delta Z \\ \delta m \\ \delta \nu \end{bmatrix} = \begin{bmatrix} 1 & 0 & 0 & 0 & 0 \\ 0 & 1 & 0 & 0 & 0 \\ 0 & 0 & 1 & 0 & 0 \\ 0 & 0 & 0 & 1 & 0 \\ \frac{1}{\dot{\nu}} \cdot \frac{\partial \nu}{\partial x_0} & 0 & \frac{Z_0}{\dot{\nu}} \cdot \frac{\partial \nu}{\partial Z_0} & \frac{m_0}{\dot{\nu}} \cdot \frac{\partial \nu}{\partial m_0} & \frac{\dot{\nu}_0}{\dot{\nu}} \cdot \frac{\partial \nu}{\partial \nu_o} \end{bmatrix} \cdot \begin{bmatrix} x_0 \\ x_0' \\ \delta Z_0 \\ \delta m_0 \\ \delta \nu_0 \end{bmatrix} \tag{32}$$

In this transformation coordinates, angles, masses, and ionic charge states are preserved. Angular scattering and energy straggling are neglected. The elements in the fifth line can be obtained from the energy-range relation, whereby the shape of the profiled degrader is taken into account. For relativistic particles the matrix coefficients are obtained from numerical calculations of the energy loss, at intermediate energies a simple approximation for the energy-range relation may be used:

$$r = k \cdot \frac{m}{Z^2} \cdot \nu^\lambda \tag{33}$$

The constants k and λ depend on the stopping material, e.g. the range of intermediate-energy ions (mass number A, nuclear charge Z) in aluminum may be estimated by the following relation:

$$r \approx 140 \frac{A}{Z^2} \nu^{3.5} \quad g/cm^2 \tag{34}$$

In this approximation, the energy loss in a degrader can be expressed by the difference in ranges of the particles before and after having passed the degrader:

$$\nu = \nu_o \cdot (1 - \frac{\hat{d} + \alpha x}{k\, m\, \nu_o^{\lambda}} Z^2)^{1/\lambda} \tag{35}$$

Here we have used a wedge-shaped degrader of the thickness $d = \hat{d} + \alpha \cdot x$, $\hat{d}$ being the thickness at the optical axis, α is the wedge angle. From eq. (35), the elements of the degrader matrix are obtained as:

$$\frac{1}{\hat{\nu}} \cdot \frac{\partial \nu}{\partial x_o} = \frac{-\alpha}{\lambda(r - \hat{d})} \qquad \frac{\hat{\nu}_o}{\hat{\nu}} \cdot \frac{\partial \nu}{\partial \nu_o} = \frac{r}{(r - \hat{d})}$$

$$\frac{Z_o}{\hat{\nu}} \cdot \frac{\partial \nu}{\partial Z_o} = \frac{-2d}{\lambda(r - \hat{d})} \qquad \frac{m_o}{\hat{\nu}} \cdot \frac{\partial \nu}{\partial m_o} = \frac{\hat{d}}{\lambda(r - \hat{d})} \tag{36}$$

We consider now the particle coordinates [X_3] at the end of the whole separator which consists of two focusing and dispersive separator stages described by the matrices [M_1] and [M_3], and the wedge-shaped degrader represented by the matrix [W_2]:

$$[X_3] = [M_3] \cdot [W_2] \cdot [M_1] \cdot [X_o] \tag{37}$$

The subscripts 1, 2 and 3 refer to the first separator stage and its image plane, the intermediate energy degrader and the coordinates at its exit plane, and to the second separator stage and its image plane, respectively. In order to obtain an optimum charge and mass resolution also for a wide velocity spread of the particles to be separated, the velocity dispersion of the whole system has to be zero. From equation (37) follows:

$$D_1 = -\frac{D_3}{V_3}\left(D_1 \cdot \frac{\partial \nu_2}{\partial x_1} \cdot \frac{1}{\hat{\nu}_2} + \frac{\partial \nu_2}{\partial \nu_1} \cdot \frac{\hat{\nu}_1}{\hat{\nu}_2}\right) \tag{38}$$

The well-known condition for the magnetic achromat is:

$$D_3 = -D_1 \cdot V_3 \tag{39}$$

Hence, if an absorber is introduced into an achromatic system, which represents a very special case of equation (38), the absorber must be wedge shaped to match the dispersions:

$$\frac{\partial \nu_2}{\partial x_1} = \frac{\hat{\nu}_2}{D_1} \cdot \left(1 - \frac{\partial \nu_2}{\partial \nu_1} \cdot \frac{\hat{\nu}_1}{\hat{\nu}_2}\right) \tag{40}$$

According to equation (38), any two-stage separator can be used as momentum-loss separator. The dispersion matching can either be fulfilled by an appropriate shape of the degrader or with appropriately setting the quadrupoles to match the dispersions at the degrader. The advantage of the achromat is its high symmetry, which is favourable if higher-order aberrations have to be kept small.

In general, the profiled intermediate degrader preserves the achromaticity exactly for only one isotope. The achromaticity condition is also approximately fulfilled for neighbouring nuclei. It should also be noted that a wedge-shaped degrader is not suited for a high-resolution operation. Higher-order corrections to the profile are thus indispensable.

4.2.3 Operation Domain of the Bρ-Δp Separation Method

The Bρ-Δp separation method works best in a limited energy domain. On the one hand, the energy must be sufficiently high in order to ensure that the fragments are totally stripped because different charge states would cause ambiguities in the magnetic separation. On the other hand, there is also an upper limit for the energy of the beam due to secondary nuclear reactions in the thick intermediate degrader. Secondary reactions are the origin of cross contaminations at the exit of the system and they reduce the intensity of the selected isotope. The estimated operation domain of the Bρ-Δp separation method is indicated in fig. 4.3.

The energy, corresponding to a portion of 50 % fully stripped ions, was calculated by the condition, that the cross section σ_{capt} of the fully stripped ion to capture an electron is equal to the cross section σ_{loss} of the one-electron system to loose its electron. The evaluations of σ_{capt} and σ_{loss} are described in section 3.

The loss of fragments due to secondary reactions in the degrader can be expressed by a nuclear absorption coefficient μ:

$$\mu = \frac{N_A}{A_d}(\sigma_{Nuc} + \sigma_{ED}) \qquad (41)$$

N_A is the Avogadro constant and A_d is the mass number of the degrader material. The estimations of the total cross sections σ_{Nuc} and σ_{ED} for nuclear reactions and electromagnetic dissociation are given in section 3. The upper curve in fig. 4.3 represents the energy which fulfills the following condition:

$$e^{-\mu \cdot d} = 1/2 \quad with \quad d = r_f/2 \qquad (42)$$

In the following sections it will be shown that a good resolution of the separator is acheaved with a degrader thickness d of about half the range r_f of the selected fragment in the degrader material. The range r_f depends strongly on the energy of the fragments, while the absorption coefficient μ is nearly constant as long as the electromagnetic dissociation can be neglected. In this case, the corresponding 1/e thickness of a fragment with mass number A_f in a degrader material with mass number A_d can be estimated by the relation:

$$1/\mu \approx 40 \cdot \frac{A_d}{(A_d^{1/3} + A_f^{1/3})^2} \quad g/cm^2 \tag{43}$$

Both μ and r_f depend on the degrader material. In order to minimize the loss of fragments during the slowing-down process, the ratio of the electronic interactions relative to the nuclear reactions must be maximized. Roughly speaking, this implies that the parameter $Z_d/A_d^{2/3}$ of the degrader material should be as large as possible. For heavy fragments above 1 GeV/u, the Z of the most favourable degrader material is reduced by electromagnetic dissociation.

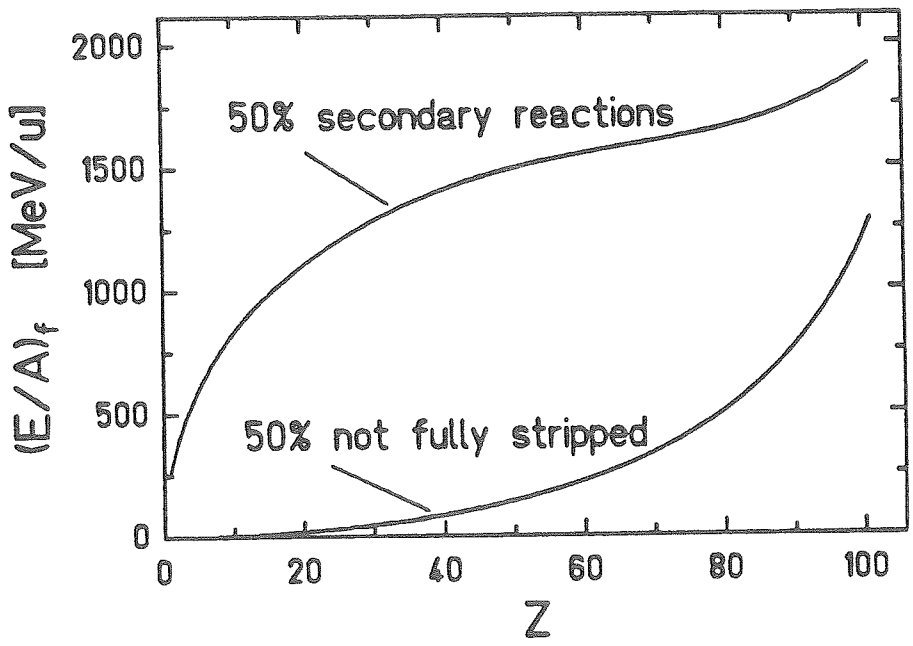

Fig. 4.3: The energy domain for the Bp-Δp separation method as a function of the fragment nuclear charge: ionic-charge limit and nuclear cross-section limit. The ordinate is the energy per nucleon of the fragment at the entrance of the degrader. If the target is not too thick, this energy differs only little from the projectile energy. The lines shown correspond to a 50 % portion of not fully stripped ions and to a 50 % loss due to secondary reactions in the lead intermediate degrader. The thickness of the intermediate degrader is assumed to be 50% of the range of the selected fragment.

There is a large energy range from several tens of MeV/u to 1 GeV/u, where the Bρ-Δp method can be applied for separating light ions. For heavier ions up to uranium the optimum energy is about 1 GeV/u which is already a compromise of accepting a portion of not completely stripped ions on the one hand and some loss of the selected projectile fragment due to nuclear reactions in the intermediate degrader on the other hand.

4.2.4 Optimisation of the Target Thickness

As already pointed out in ref. [DUF86], there exists an optimum target thickness for which the intensity of a particular isotope at the exit of the momentum-loss achromat is maximum. If the target becomes thinner, the production rate is reduced, for a thicker target the slowing-down effects broaden the distributions in momentum and angle and the transmission through the separator is reduced. At relativistic energies, the ranges of projectiles and fragments in matter are high and the straggling effects are small. Therefore very thick targets in the order of several g/cm^2 become available. But in this case the optimum target thickness is additionally limited by the loss of fragments in the target due to the increasing probability for secondary reactions.

The number of fragments n_f of a special isotope per incident projectiles n_p, produced by a single reaction in the target, is given by

$$\frac{n_f}{n_p} = \frac{N_A \cdot \sigma_f}{A_t(\mu_f - \mu_p)}\left(e^{-\mu_p t} - e^{-\mu_f t}\right) \qquad (44)$$

t is the target thickness, σ_f the production cross section for the selected fragment and A_t the mass of the target atoms. μ_p and μ_f are the absorption coefficients of projectiles and fragments, respectively, in the target:

$$\mu = \frac{N_A}{A_t}(\sigma_{Nuc} + \sigma_{ED}) \qquad (45)$$

The optimum target thickness t_{opt} is given by the maximum of the product of n_f / n_p and the transmission T of the selected fragment through the separator. We define the effective optimum target thickness t_{eff} as the corresponding, effectively

used target thickness for the intensity of projectile fragments at the exit of the separator:

$$t_{eff} = T \cdot \frac{e^{-\mu_p t_{opt}} - e^{-\mu_f t_{opt}}}{\mu_f - \mu_p} \tag{46}$$

With this definition, the number $T \cdot n_f$ of fragments leaving the separator is:

$$T \cdot n_f = t_{eff} \cdot \sigma_f \cdot n_p \cdot N_A / A_t \tag{47}$$

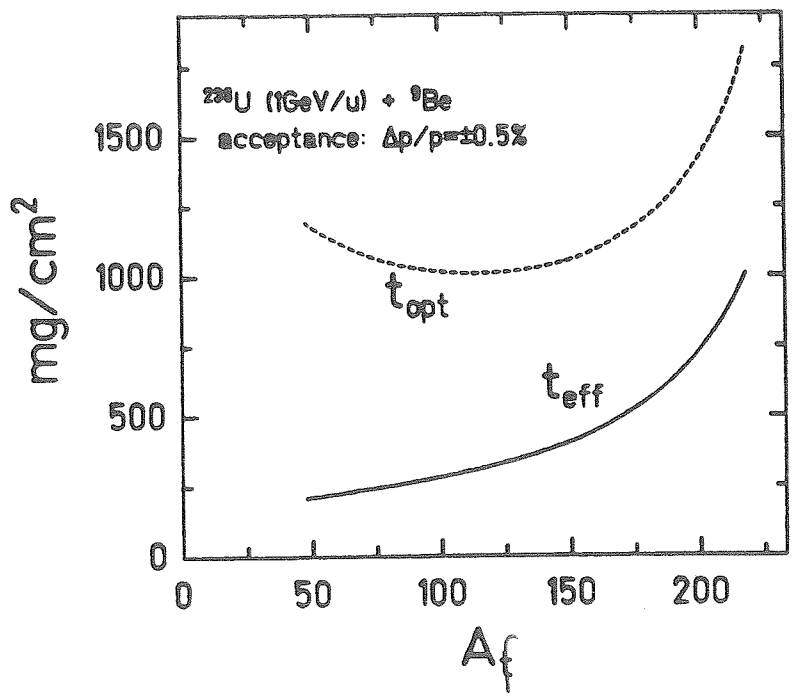

Fig. 4.4: Optimum and corresponding effective target thickness as a function of the target mass number. Dashed line: Optimum target thickness t_{opt} which provides the highest rate of projectile fragments at the intermediate focal plane of the momentum-loss achromat. Full line: Effective optimum target thickness t_{eff} . The N/Z ratio is fixed at a value which is 2.5 % above that of the projectile ^{238}U. The transmission of the second stage of the separator is assumed to be one.

In contrast to the situation discussed above for the degrader, in the target a high nuclear cross section and a low energy loss of projectile and fragment is desired. Therefore, the intensity $T \cdot n_f$ is maximum if a light target-material is used.

The variations of t_{opt} and t_{eff} as a function of the fragment mass are shown in fig. 4.4. For calculating the transmission of the separator, a momentum acceptance of $\Delta p/p = \pm 0.5$ % and an angular acceptance of 15 mrad was assumed. The target thickness has little influence on the transmission through the second dipole section if its acceptance is equal to that of the first one. In the case of a thin intermediate degrader the transmission is close to one.

Fig. 4.4 shows some general features. The effective optimum target thickness t_{eff} decreases rapidly with increasing mass difference between projectile and fragment. The reason is the increasing momentum spread due to the reaction mechanism and the energy-loss difference of projectiles and fragments in the target. In this special example, the transmission through the separator decreases from about 80% at A = 200 to 20% at A = 30. For fragments with little mass difference to the projectiles, the effective target thickness is limited by multiple reactions in the target. As a conlusion from fig. 4.4, fragment beams should be produced by primary beams which are as similar as possible to the desired fragments in order to maximize the effective target thickness.

Fig. 4.5 shows the optimum and the corresponding effective target thickness as a function of the projectile energy. The presented example is again the production of a neutron-rich heavy nucleus, but it holds also true for light fragments, that the optimum and the effective target thickness increase with the projectile energy until they reach finally the saturation. Then the transmission through the first stage of the separator is nearly 100 %, and the optimum target thickness approaches the value for which n_f/n_p (equation 44) reaches its maximum. The ratio t_{eff}/t_{opt} is about 0.4 at saturation. The saturation energy, however, lies outside the operation domain of the momentum-loss achromat (see fig. 4.3).

The relative momentum widths due to the reaction kinematics and due to the energy loss depend on the projectile energy in a different way. The contribution of the reaction is proportional to $1/p_z$, and the energy-loss contribution increases with t/r_f. Therefore, the reaction kinematics is decisive at low energies, while the energy loss is dominant at higher energies.

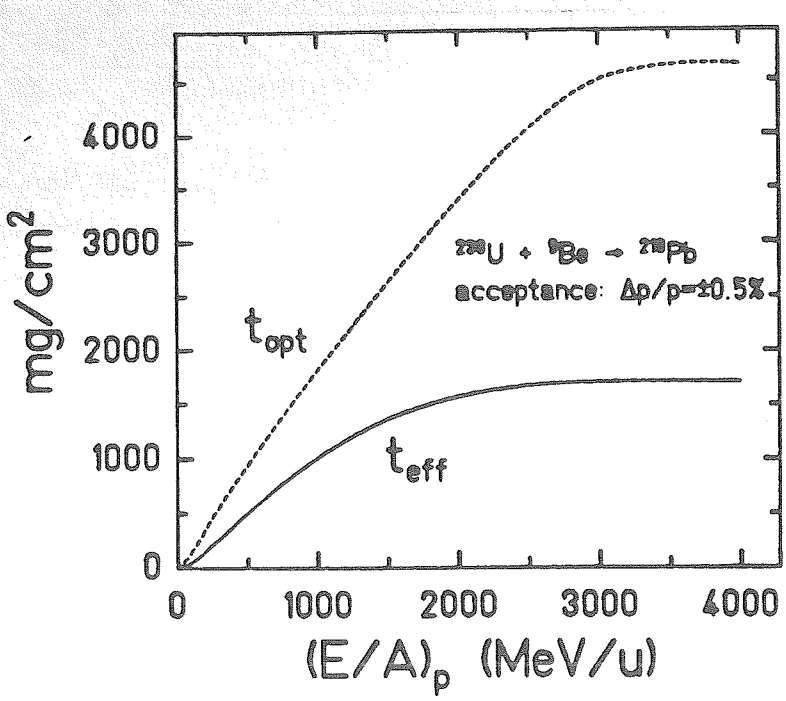

Fig. 4.5: Optimum and corresponding effective target thickness as a function of projectile energy. Dashed line: Optimum target thickness t_{opt} which provides the highest rate of projectile fragments at the exit of the momentum-loss achromat. Full line: Effective optimum target thickness t_{eff}. The transmission through the second separator section is assumed to be one.

4.2.5 Selection Characteristics

The momentum-loss achromat consists of two sections. The first section has two tasks: Firstly, it separates fully stripped ions according to their A/Z ratio with a resolution, determined by their momentum width. Secondly, the momentum dispersion in the intermediate focal plane is adapted to the profile of the thick intermediate degrader so that the resolving power at the exit of the whole system is high and independant of the momentum width of the ions.

If there are no ionic-charge-exchange processes and no nuclear reactions in the degrader, the deflection at the exit of the momentum-loss achromat can be calculated from equation (37) by inserting the appropriate matrix elements. For a spectrometer which is achromatic without wedge and $x_0 = 0$, we get:

$$x_3 = D_3 \cdot (\delta\nu_2 - \delta\nu_1) \tag{48}$$

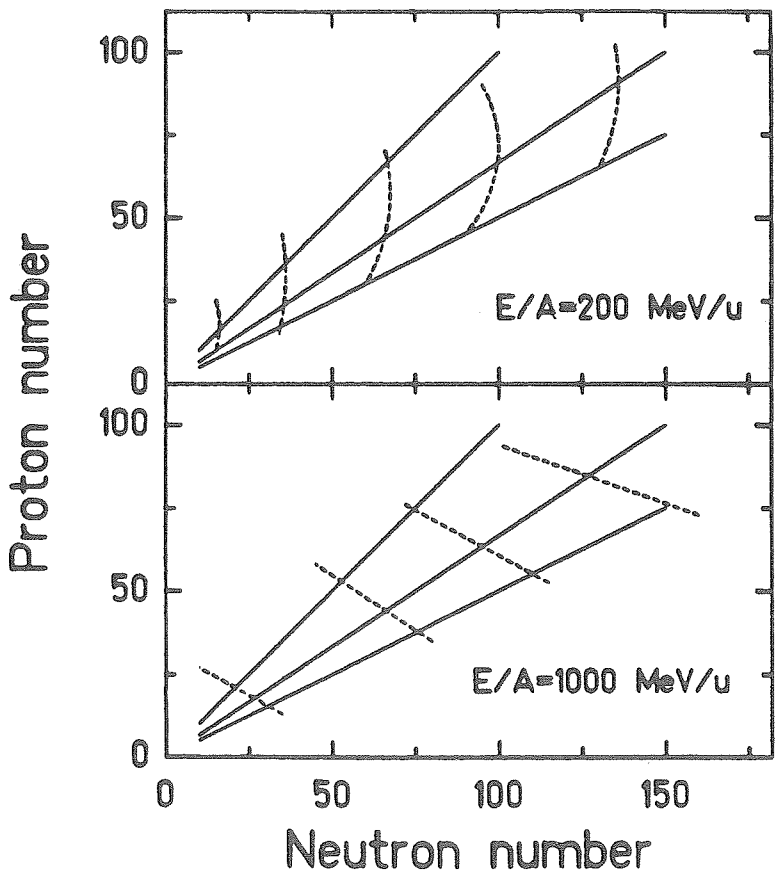

Fig. 4.6: Examples for the lines corresponding to the two selection criteria of the momentum-loss achromat on the chart of nuclides. Full lines: first selection for different $B\rho_1$ values. Dashed lines: second selection for different settings of d and $B\rho_3/B\rho_1$. The curves are calculated for beams of 200 MeV/u and 1000 MeV/u ^{238}U, a beryllium target with a constant relative thickness $t/r_p = 0.15$ and an aluminum intermediate degrader with $d/r_f = 0.5$.

Note that $v_0 = v_1$ and $v_2 = v_3$. It may be instructive to write equation (48) as follows:

$$x_3 = D_3 \frac{\nu_1}{\hat{\nu}_2} \left[\frac{\nu_2}{\nu_1} - \frac{\hat{\nu}_2}{\hat{\nu}_1} \right] \approx \frac{D_3}{\eta} \left[\frac{\nu_2}{\nu_1} - \eta \right] \tag{49}$$

The selection criterion is the ratio of the momenta of the individual isotopes before and behind the degrader. By imposing a certain value $\eta = \hat{v}_2/\hat{v}_1$ by the strengths of the dipole fields, nuclei with a fixed momentum ratio η are selected.

The two selection criteria are met by the projectile fragment lying on two intersecting lines on the chart of nuclides. Some examples for the positions of these lines for different settings as obtained by numerical calculations are shown in fig. 4.6 for two energies. The position of the first selection line varies with $B\rho_1$, that of the second selection with the degrader thickness d and the ratio $B\rho_3/B\rho_1 = \eta$. The slopes of the lines of the second selection turn counterclockwise with increasing energy. The influence of the degrader thickness on the slope is only weak.

4.2.6 The Resolution of the Momentum-Loss Achromat

The widths of the two kinds of selection lines as descriped in the previous section result from two different contributions: physical processes which can be optimized to some extend by the operation conditions and the limit due to the ion-optical quality of the system. An overview is given in table 4.3.

The resolution of the momentum-loss achromat is the result of many different contributions. It was calculated by the extended ion-optical model of multidimensional distributions as described above. Let us first consider the physical limits of the method. The minimum width of the first selection for a thin target and an ideal instrument is given by:

$$\frac{\sigma(A/Z)}{A/Z} = \frac{\sigma(p_{\|})}{p_{\|}} \tag{50}$$

According to the Goldhaber approach, $\sigma(p_{\|})$ does not vary with energy. Therefore the resolving power increases with the momentum of the projectiles. Moreover, the resolution ist best if the mass difference between fragment and projectile is as small as possible.

The second selection is a more complex process. Numerical calculations of the physical limit for the second selection with an ideal instrument can be parametrized by a gaussian distribution perpendicular to the selection lines (fig. 4.6) with a standard deviation as given by the following fit formula:

$$\sigma(\chi) = (3.5 \pm 1) \cdot 10^{-3} \cdot \sqrt{Z_f \cdot r_f / d} \tag{51}$$

χ stands for the distance between two points on the chart of nuclides (fig. 4.6); e.g. the α decay corresponds to $\chi = 2 \cdot \sqrt{2}$. The numerical calculations revealed, that the resolution is nearly independant of the degrader material. The deviations of $\sigma(\chi)$ from (29) with beam energy and Z_f do not exceed the indicated spread of about $\pm$ 30 %, if one stays inside the operation domain of the method (fig. 4.3).

Fig. 4.7 shows the transmission values of a selected isotope and of the cross contaminants on a chart of nuclides for different operation conditions. Secondary reactions and charge-changing processes are neglected and will be discussed in the next section. This is a more detailed study of the example already presented in fig. 4.2. The background at the exit of the momentum-loss achromat is strongly influenced by the slope of the second selection lines. At projectile energies near 1 GeV/u, the

selected quantity	physical processes	apparativ contributions	relevant operation parameters
$\approx A/Z$	**reaction kinematics** energy loss $(\Delta E_p - \Delta E_f)$ energy straggling in the target	magnetic resolution $(\Delta B\rho/B\rho)_1$	E_p (a) $\sigma(p_p)$ (b) t/r_p (c) $A_f - A_p$ (d)
relative momentum p_2/p_1	**energy straggling** **in the intermediate** **degrader**	magnetic resolutions $(\Delta B\rho/B\rho)_1$, $(\Delta B\rho/B\rho)_3$ $\sigma(d)/d$ (g)	d/r_f (e) E_p (f)

Table 4.3: The resolution-determining conditions of the momentum-loss achromat
Remarks: (a) Projectile energy. (b) Momentum width of the beam. (c) Target thickness relative to the range of the projectiles. (d) Mass difference of fragment and projectile. (e) Degrader thickness relative to the range of the selected fragment. (f) The projectile energy nearly does not change the resolution width but it modifies the slope of the resolution lines (fig. 4.3). (g) Inhomogeneity or inadequate profile of the intermediate degrader. The magnetic resolution ($\Delta B\rho/B\rho$) includes the contribution due to the emittance of the projectile beam. The influence on the isotope separation of the processes printed in boldface cannot be reduced below a certain level.

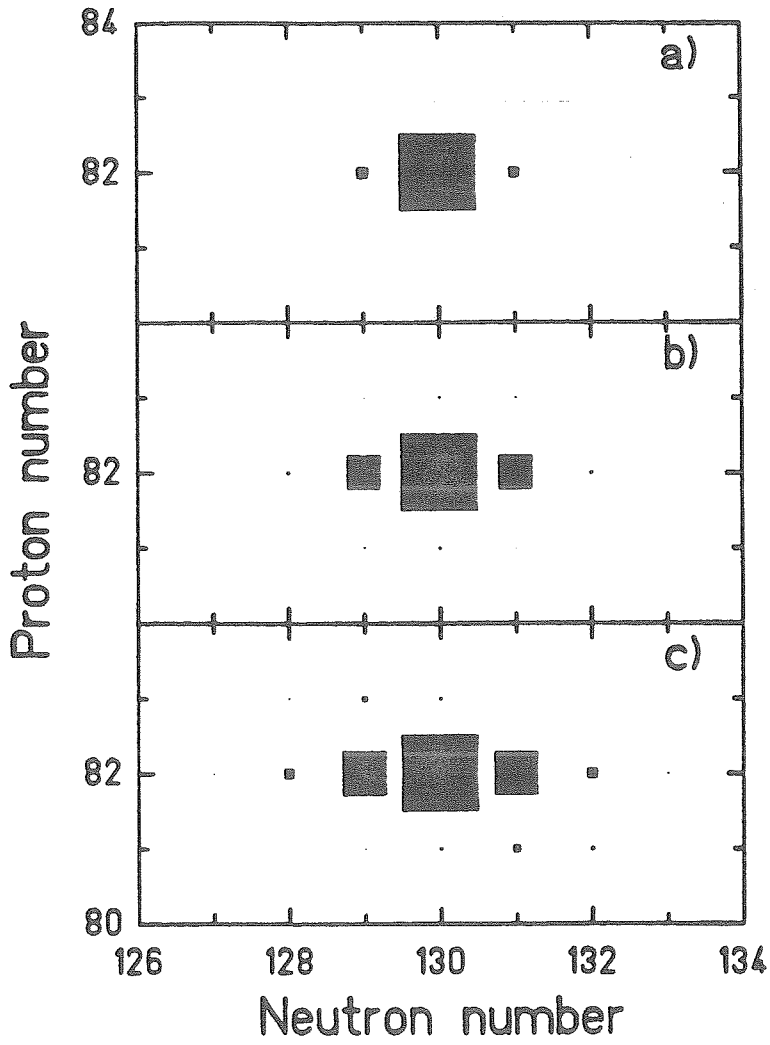

Fig. 4.7: Transmission values of the momentum-loss achromat for a selected projectile fragment and the contaminents on a chart of nuclides (^{238}U, 1000 MeV/u → ^{9}Be, lead degrader, $d/r_f = 0.3$). Charge-changing processes and secondary nuclear reactions are neglected. The area of the symbols is proportional to the transmission value.

(a) Physical resolution limit, obtainable under ideal operation conditions.

(b) Transmission pattern for good but realistic operation conditions: $t/r_p = 0.05$, momentum width of the beam $\sigma(p_p)/p_p < 10^{-3}$, magnetic resolution $B\rho/\Delta B\rho = 1500$, inhomogeneity of the intermediate degrader $\sigma(d)/d < 10^{-3}$.

(c) Transmission pattern when the target thickness is chosen to yield the maximum intensity of ^{212}Pb ($t/r_p = 0.14$).

neighbouring isotopes are the most important contaminants. The situation as shown in fig. 4.7 is probably the most difficult case one can imagine for the task to separate relativistic projectile fragments.

In general, the resolution quality becomes better by increasing the thickness of the intermediate degrader up to a value around 80% of the range of the fragments. For heavy fragments, however, the degrader thickness is limited by the occurrence of ionic charge-changing processes.

The energy straggling in the intermediate degrader is the final resolution-limiting condition of the second selection of the momentum-loss achromat. This resolution limit can only be attained, if the technical quality of the device is high. Table 4.4 gives the aberrations of the two dipole sections and the inhomogeneity of the degrader which cause the same width $\sigma(x_3)$ as the energy straggling. For the final resolution, the individual contributions add quadratically.

In table 4.4, the projectile is only important in so far as it determines the velocity of the selected fragment. Therefore only the data for ^{238}U are given. According to the calculation, the second dipole section is less critical than the first one. The highest magnetic resolution is required for the heaviest fragment and the thinnest intermediate degrader. In a very critical condition for a beam of ^{238}U with 1000 MeV/u, the heavy fragment ^{234}Ac, and a value $d/r = 0.3$, a resolution of $B\rho/\Delta B\rho \approx 2000$ is equivalent to the influence of the straggling. (Here for $\Delta B\rho$ the FWHM is taken.) The intermediate profiled degrader must be constructed with a rather high precision of a few µm in order not to deteriorate the resolution.

The physical resolution limit as calculated with the relations for the energy straggling given in section 3 can only be reached, if the aberrations of the system keep appreciably below the equivalent resolution parameters as given in table 4.4. If the technical quality of the system is not excellent, the resolution is not limited by the straggling phenomena at all.

Proj.	E/A Mev/u	t/R_p (a)	d/R_f (b)	Fragm.	$(\sigma(p)/p)_1$ (c)	$(\sigma(p)/p)_3$ (d)	$\sigma(d)/d$ (e)	d g/cm^2 (f)
^{238}U	1000	0.1	0.1	^{234}Ac	$1.2 \cdot 10^{-4}$	$1.3 \cdot 10^{-4}$	$2.5 \cdot 10^{-3}$	1.0
^{238}U	1000	0.1	0.3	^{234}Ac	$2.0 \cdot 10^{-4}$	$2.7 \cdot 10^{-4}$	$1.4 \cdot 10^{-3}$	3.1
^{238}U	1000	0.1	0.3	^{155}Nd	$2.5 \cdot 10^{-4}$	$3.3 \cdot 10^{-4}$	$1.7 \cdot 10^{-3}$	4.7
^{238}U	1000	0.1	0.5	^{155}Nd	$3.1 \cdot 10^{-4}$	$5.5 \cdot 10^{-4}$	$1.3 \cdot 10^{-3}$	7.9
^{238}U	200	0.1	0.5	^{155}Nd	$2.6 \cdot 10^{-4}$	$4.9 \cdot 10^{-4}$	$1.5 \cdot 10^{-3}$	0.73

Table 4.4: Resolution parameters of the momentum-loss achromat which are equivalent to the energy straggling in an aluminum intermediate degrader:

(a) target thickness relative to the range of the projectiles;

(b) degrader thickness relative to the range of the selected fragment;

(c) resolution of the first dipole section, including the contribution due to the size of the beam spot at the target position;

(d) resolution of the second dipole section alone for a point source of fragments in the intermediate focal plane;

(e) deviations from the ideal thickness of the intermediate degrader;

(f) thickness of the intermediate degrader.

The quantities in the first five columns are initial values of the calculation. Note that the standard deviations are given!

In this case, the resolutions R_m and R_Z of the second selection of the momentum-loss achromat for constant Z and for constant m can be calculated in the first-order matrix description:

$$R_m = \frac{D_1}{x_0 V_1} \frac{\frac{m_1}{\nu_2}\frac{\partial \nu_2}{\partial m_1} - \frac{\nu_1}{\nu_2}\frac{\partial \nu_2}{\partial \nu_1} + 1}{\frac{\nu_1}{\nu_2}\frac{\partial \nu_2}{\partial \nu_1}} \qquad for\ Z = const. \tag{52}$$

$$R_Z = \frac{D_1}{x_0 V_1} \frac{\frac{Z_1}{\nu_2}\frac{\partial \nu_2}{\partial Z_1} - \frac{\nu_1}{\nu_2}\frac{\partial \nu_2}{\partial \nu_1} + 1}{\frac{\nu_1}{\nu_2}\frac{\partial \nu_2}{\partial \nu_1}} \qquad for\ m = const. \tag{53}$$

The important result of these equations is that generally for momentum-loss achromates the resolution is a product of the net resolution of the spectrometer $R_1 = D_1/x_0 \cdot V_1$ and the "differential velocity losses" for a given initial velocity, charge or mass, respectively. From the non-relativistic approach of equation (34) we obtain for an aluminum absorber of half-range thickness

$$R_m = 0.36 \cdot R_1, \qquad R_Z = 0.21 \cdot R_1 \tag{54}$$

The slope of the second selection lines $\Delta Z/\Delta A$ is related to the projected resolutions:

$$\frac{\Delta Z}{\Delta A} = \frac{Z}{A} \cdot \frac{R_Z}{R_m} \tag{55}$$

4.2.7 Cross Contaminants due to Charge-Changing Processes and Secondary Reactions

If the energy of the fragments is not sufficiently high, they may not be fully stripped. The different charge states give rise to an ambiguity due to different deflections in the two magnetic dipole sections. Figure 7 shows the transmission values of the momentum-loss achromat for the charge states q = Z, Z-1 and Z-2 in the second dipole section.

Nuclear reactions which are necessary to form projectile fragments in the target are inconvenient in the intermediate degrader because they reduce the intensity of the selected fragment and produce additional background. It is particularly important to take care that the primary beam does not hit the intermediate degrader. Otherwise a large amount of secondary reaction products would be created which could cause a high level of cross contaminants at the exit of the separator.

The products of secondary reactions in the intermediate degrader with a different magnetic rigidity are suppressed by the magnetic selection in the second dipole section. If the projectile fragments are to be stopped at the exit of the momentum-loss achromat, their range can be used as an additional selection criterion. The final degrader is devided in two sections, a predegrader and a catcher foil. The catcher foil covers just the range distribution of the selected isotope. Products with smaller range are stopped in the predegrader while products with larger range pass through the catcher. As already pointed out in ref. [DUF86], the range and the total deflection in the momentum-loss achromat select about the same nuclei at intermediate energies. For higher energies the slopes of the selection lines are slightly different.

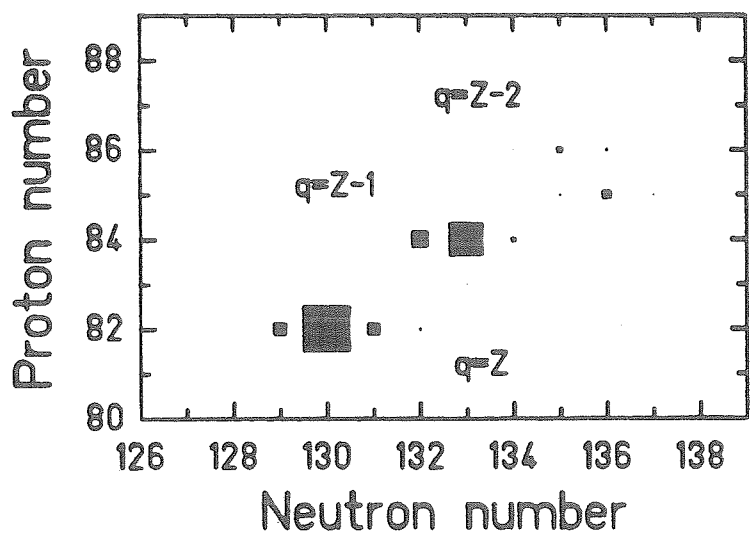

Fig. 4.8: Example for the tansmission pattern for different charge states (q = Z, q = Z-1 and q = Z-2) in the second dipole section. It is assumed that the ions are fully ionized before reaching the degrader. (1000 MeV/u ^{238}U + ^{9}Be, $t/r_p = 0.05$, $d/r_f = 0.5$)

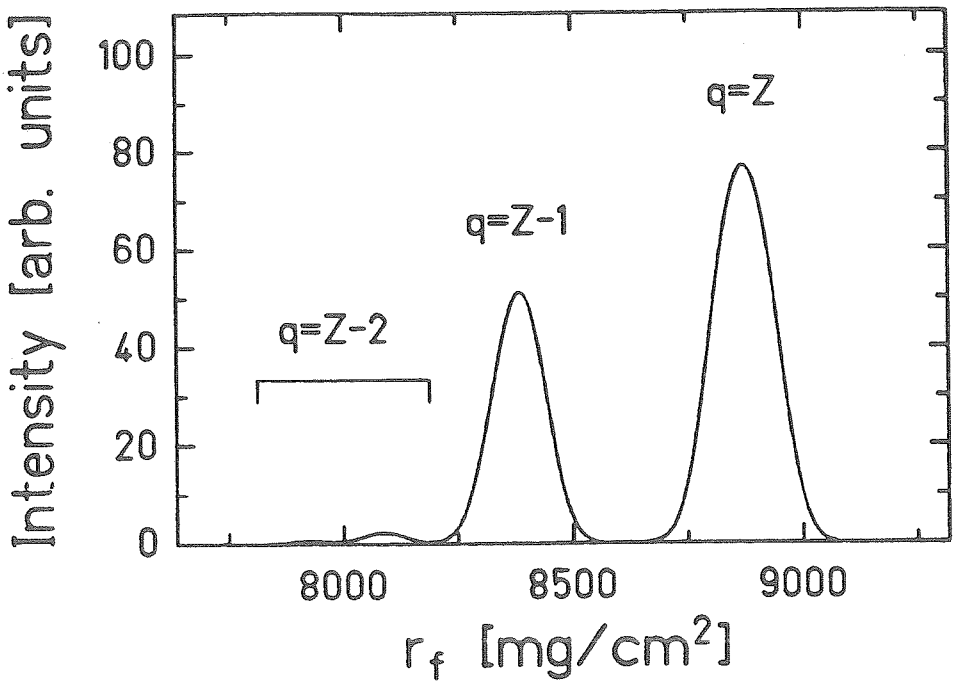

Fig. 4.9: Range distribution of the isotopes shown in fig. 4.8 in a lead stopper at the exit of the separator. A range selection is able to suppress cross contaminants due to different charge states in the second dipole section of the momentum-loss achromat. Range straggling is included.

If different ionic charge states pass through the device, the range selection is much more useful. Fig. 4.9 shows the range distributions of the isotopes which leave the momentum-loss achromat in the example shown in fig. 4.8. Another application of the range selection is the suppression of secondary reaction products. As the fragmentation process conserves approximately the projectile velocity, the nuclei with A/Z^2 values different from that of the selected isotope can be suppressed by a range selection. Especially all light nuclei which are produced with high cross sections are discriminated by their larger ranges. If instead of an achromatic intermediate degrader a monokinetic shape is used, the range distribution of the selected fragment is compressed and the range resolution is increased.

4.2.8 The Emittance of the Fragment Beam

The phase-space volume of the fragment beam at the exit of the separator is determined by the phase-space of the projectile beam and by additional contributions due to the nuclear reactions in the target and slowing-down processes in the target and in the intermediate degrader including angular and energy-loss straggling.

In the first-order approximation, the phase space of the fragment beam behind the target is directly related to that at the exit of the separator. The magnetic dipole sections do not alter the phase-space volume. Therefore, only the influence of the degrader has to be considered. The phase-space transformation at the absorber can be calculated from the transformation of the six-dimensional σ ellipsoid, the absorber matrix, and its transposed [BRO70]:

$$\sigma = [W] \cdot [\sigma_0 \cdot] \cdot [W]^T \tag{56}$$

As we are interested in a certain isotope with fixed rest mass and ionic charge, we have $\delta p_z = \delta v$. The other coordinates are x, x′, y, y′ and Δz. We obtain the emittance behind the absorber:

$$\epsilon = \sqrt{det(\sigma)} \tag{57}$$

The enlargement of the emittance is given by:

$$\epsilon = \frac{\nu_1}{\nu_2} \cdot \frac{\partial \nu_2}{\partial \nu_1} \cdot \frac{\Delta z_2}{\Delta z_1} \epsilon_0 \tag{58}$$

which is in the non-relativistic approach with the analytic parametrization of the range relation:

$$\epsilon = \frac{p_{z1}^{\lambda-1}}{p_{z2}^{\lambda-1}} \cdot \epsilon_0 = \frac{r_{f1}}{r_{f2}} \cdot \frac{\Delta z_2}{\Delta z_1} \cdot \epsilon_0 \tag{59}$$

This enlargement of the emittance is quite moderate.

The question how the enlargement of the emittance influences the transversal x phase space can be answered as follows: As Δz does not couple to the other coordinates, the two coordinates x and δv are closely related:

$$x_3 \cdot \delta\nu_3 = x_0 \cdot \delta\nu_0 \cdot \frac{\partial\nu_2}{\partial\nu_1} \cdot \frac{\hat{\nu_1}}{\hat{\nu_2}} \tag{60}$$

In the monochromatic mode, a reduction of the velocity spread by some factor causes an enlargement in x direction by the same factor. This can be easily understood: The contribution to the beamspot at the degrader is given by the velocity dispersion D_1 of the first stage and the velocity spread $\delta v_1 = \delta v_0$:

$$x_2 = D_1 \cdot \delta\nu_0 \tag{61}$$

The degrader is shaped as to compress this velocity band of initial width δv_0 which for the second stage gives a monochromatic source of the width x_2. The exit velocity spread is given by the velocity gradient in x direction along the degrader and the beamspot size.

$$\delta\nu_2 = V_1 \cdot x_0 \cdot \frac{\partial\nu_2}{\partial x_1} \cdot \frac{1}{\hat{\nu_2}} \tag{62}$$

These first-order considerations have to be completed by including the effects of the nuclear reactions in the target as well as the angular and the energy-loss straggling in the target and in the intermediate degrader. For a beam energy of about 1 GeV/u, these effects cause additional widths in the order of

$$\delta\nu \approx 10^{-3} \qquad and \quad x' \approx 5 \cdot 10^{-3} \tag{63}$$

4.2.9 Summary

The Bρ-Δp separation method is applicable in a wide energy range and for all nuclei up to uranium. This operation domain is well adapted to the specifications of SIS18. The separation time is determined only by the time-of-flight of the fragments through the system. The transmission of the separator is in the order of 50 %, independent of the chemical properties of the selected isotope.

The condition that heavy isotopes are fully stripped during their passage through the whole separator requires a magnetic field strength of $B\rho \approx 18$ Tm.

The isotopical resolving power depends strongly on the resolution of the magnetic system. The magnetic resolution must reach at least a value of $B\rho/\Delta B\rho = 1500$ if a good isotopical separation, especially for heavy nuclei, is required. Straggling phenomena are important only if the magnetic resolution exceeds a value of $B\rho/\Delta B\rho = 2000$.

5. *Design and Technical Layout*

5.1 *Ion-Optical Design of the Momentum-Loss Achromat*

The main design goals of the proposed magnetic system are to separate the nuclear reaction products from the primary beam and additionally to perform an efficient separation for the projectile fragments with respect to A and Z (see Sec. 4). For the operation as a momentum-loss achromat the thick production target is placed at the entrance of the separator. Due to the nuclear reaction kinematics (see Sec. 3) the projectiles and the fragments have roughly the same velocity. A velocity spread of the reaction products of 1% is caused predominantly by the thick target. This is a basic limitation for achieving a high resolving power in A/Z using only magnetic sector fields (see Sec. 4). The separation of the fragments with respect to A and Z is even more difficult, and in principle cannot be achieved with pure electromagnetic fields. Therefore, two conditions have to be met simultaneously: first to have a resolution independent of the velocity spread of the fragments and second to insert an element providing the separation with respect to A and Z. When relativistic fragments penetrate through matter, the electronic energy straggling is very small. This property allows to use a piece of matter as a special ion-optical element (see Sec. 4) for the separation of single isotopes. The problem caused by the large velocity spread of the fragments is solved using the principles of the conventional energy-loss spectrometers.

We have designed an achromatic magnetic deflection system with an absorber placed in the symmetry plane. The electronic energy loss in this thick absorber is measured with the second section of the separator. Without any precautions this would result in broad distributions at the final focal plane. The refinement is a shaped absorber to preserve the achromatism for the selected fragment [DUF86]. This fragment is then well focused and separated from possible contaminants having the same magnetic rigidity in the first stage of the momentum-loss achromat.

From these considerations it follows that the ion-optical design will concentrate on an achromatic system. The design goals are a momentum resolution of about $p/\Delta p \geq 1500$ at the position of the absorber (see chap.4), a maximum magnetic rigidity $B\rho = 18$ Tm, transmission of fragments covering a momentum spread of $\pm 1\%$ and the option to inject the radioactive beams into the storage ring ESR with proper matching. The required resolution determines the sum of the deflection angles of the

magnetic sector fields (see Sec. 4.1). The position of the synchrotron and the storage ring determines the geometrical configurations of the momentum-loss achromat .

The system has 4 stages each consisting of a 30° dipole magnet and quadrupoles providing the ion-optical imaging conditions. The momentum-loss achromat and its ion-optical scheme are illustrated in fig.5.1 .
The upper part of the fig. 5.1 shows the location of the separator in the SIS-ESR area. In part b) and c) of the figure the ion-optical elements and the particle envelopes are presented as calculated with the computer codes MIRKO and GIOS [FRA83,WOL67], respectively. In fig. 5.1b the optical elements and the beam envelopes are projected into one plane. The x-coordinate is the direction of the deflection and y is the corresponding perpendicular coordinate. The envelopes are given for a 5.397 GeV/c (18 Tm U^{92+}) beam having a horizontal and vertical emittance of 20 π mm mrad. The quadrupoles in front of the 30° dipole magnets are needed to illuminate properly the field volume of the bending magnets to achieve a high resolving power and to minimize the height of the gaps. The ion-optical conditions for the different focal planes are determined by the quadrupoles following the dipole magnets. At the first and the third foci we have required a point-to-point image in x and a waist in y direction (upright ellipse). At the position of the degrader (second focus) and for the final focus quadrupole triplets are used to achieve an image in both directions. The dotted line in fig.5.1b indicates the momentum dispersion for $\Delta p/p = 1\%$. The dispersion line demonstrates that the system is achromatic.

The optical focusing conditions are used to separate effectively the selected fragment from the primary beam and the contaminants. In our layout the high-intensity primary beam should never pass the slits (S_1) at the first focal plane and hit the degrader. At the second focus all reaction products characterized by the same selected A/Z are focused on the shaped degrader. Here we require an image in the x- and y-cordinates to minimize the emittance growth due to the multiple-scattering contributions in the degrader. The x magnification is 0.77 and the corresponding dispersion is -6.51 cm/% resulting in a first order resolution of 1526 for a spot size of 0.54 cm at the production target. This is the highest resolution we achieve for the given emittance (20 π mm mrad) and the option to transmit a 2% momentum spread of the fragments. The image size for particles with this momentum spread would be 13 cm. It is required that the dispersion line is parallel; this means that the entrance angle of the fragments at the degrader is not dependent on the momentum deviation. This condition minimizes the aberrations induced by the degrader. The third focus has the same ion optical conditions as the first one. Again, a pair of slits (S_3) is used

to reject background fragments. Our system is achromatic at the final focus. A quadrupole triplet is generating an image in x- and y- directions. The triplet is necessary for providing a flexible, stigmatic focus at the position of the experimental set-up. The size of the drift lengths at the different focal points is determined by the diagnostic elements (e.g. slits, cups, and position probes), and the particle-tracking detectors . At the symmetry plane a drift length of 5 m can be used for special experimental set-ups. In fig.5.1c the ion optical elements are shown schematically together with 18 Tm particle rays starting with three angles ($x' = 0, +7, -7$ mrad) for each of the given three different momenta ($\Delta p/p = 0, +.8, -.8\%$). The achromatism of the separator is clearly indicated at the final focal plane.
In table 5.1 and 5.2 the ion-optical specifications are summarized.

Without correcting higher-order image aberrations the first- order resolution is reduced by a factor of 3 at the intermediate focal plane. The residual resolution is then by far not sufficient for an efficient isotope separation. A significantly contaminated beam cannot be used in the ESR. Therefore higher-order aberrations must be minimized by introducing multipoles into the magnetic lattice of our first-order ion-optical design.

The corresponding ion-optical calculations are performed with the computer codes TRANSPORT and TURTLE [BRO80]. Following the description of K.L. Brown [BRO80] we have minimized the aberrations by introducing multipoles at locations where the corresponding coupling coefficients are large. Inserting sextupoles always before and after each dipole magnet, we recover more than 90% of the first-order resolution. Furthermore, the sextupole fields rotate the focal planes perpendicular to the optical axis at the position of the degrader and at the final focal plane. Before sextupole corrections were done, this angle was 11° at the degrader position.

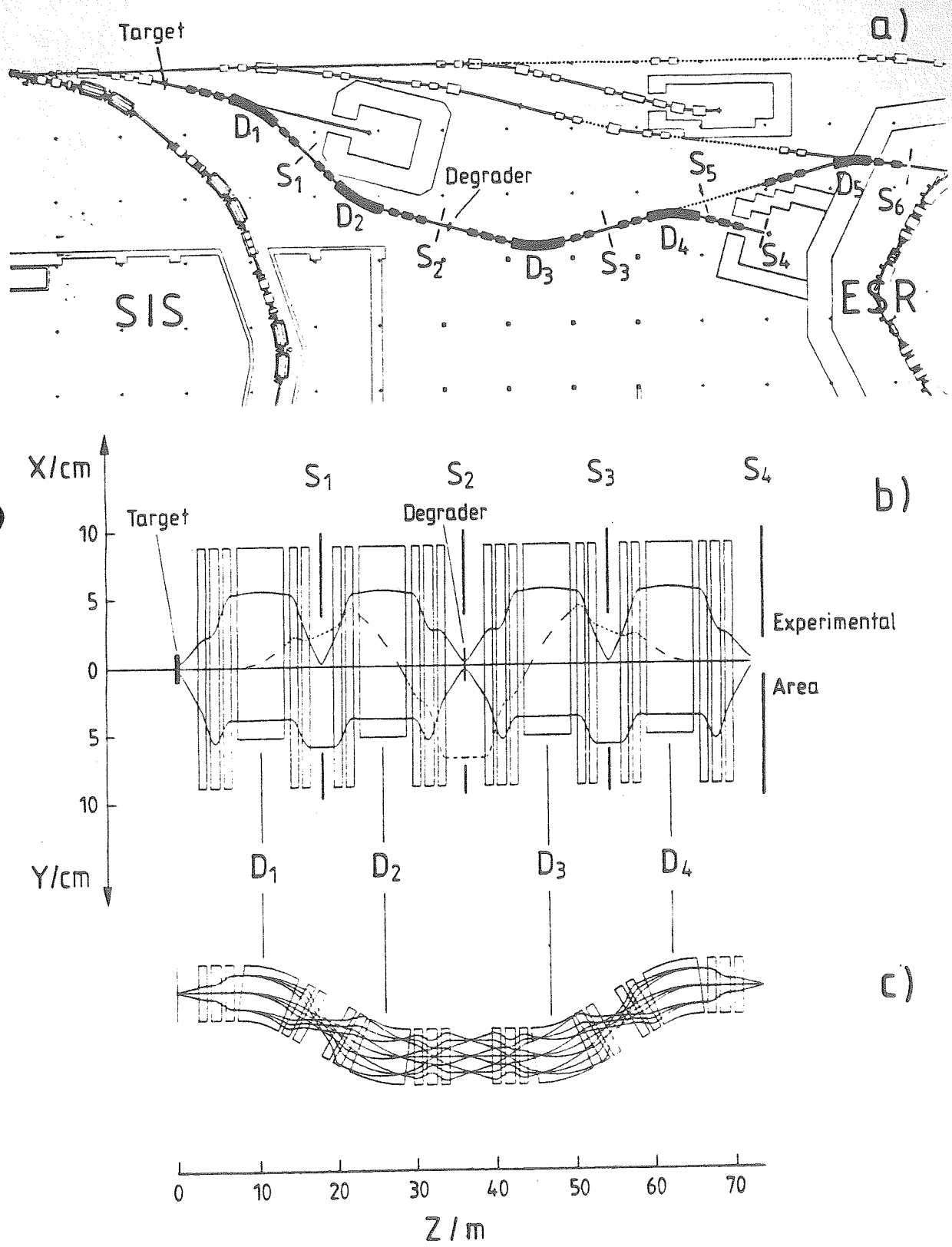

Fig. 5.1: The ion-optical layout of the momentum-loss achromat. The dipole magnets and the slits at the different focal planes are indicated by D_1-D_5 and S_1-S_6 respectively.

Table 5.1 : Global parameters of the FRS

maximum particle rigidity	B_ρ = 18 Tm
solid angle	< 0.42 msr
momentum resolution at the final focal plane	0 (achromatic)
transmission of momentum width	± 1%
distance target - final focus	74 m

Table 5.2: Ion Optical Specifications at the Focal Planes

Position	x-plane				y-plane		Resolution
	V_x	IMAGE	D cm/%	D' mr/%	V_y	IMAGE	p/Δp Δx_o = .5 cm
1. focus at 18.99 m	-0.56	yes	2.33	2.49	-3.33	no	763
2. focus at 37.18 m	0.77	yes	-6.51	0.00	-1.07	yes	1526
3. focus at 55.38 m	-0.56	yes	2.33	-2.49	8.50	no	763
4. focus at 74.37 m	1.00	yes	0.00	0.00	0.68	yes	achromatic

5.2 Injection and Storage of Radioactive Beams in the ESR

The combination of SIS, the Fragment Separator FRS and the Experimental Storage Ring ESR [FRA86] offers a new generation of unique experiments with radioactive beams, as already pointed out in Sec. 2.3. The ESR allows to store circulating beams over periods from seconds to at least some minutes, to increase the density of particles in phase space by stochastic and subsequent electron cooling either for decay studies or reactions with internal targets, as well as for extracting these highly brilliant beams. Moreover, the ESR can be used for the deceleration of the stored beams to cover a range from 500 MeV/u to 3 MeV/u.

Fig. 5.2 shows the ion-optical layout of the fragment separator to inject radioactive beams into the ESR. As in Sec. 5.1 the ion-optical elements and the beam envelopes are projected into one plane. The envelopes are given for a beam with the horizontal and vertical emittances of 20 π mm mrad. Up to the dipole magnet D_4 the ion-optical elements are identical to those described in Sec. 5.1. The dipole magnet D_4 is switched off to pass the beam through a hole in the yoke of this magnet into the transfer line to the ESR. A quadrupole triplet illuminates the 23° dipole D_5 to meet the achromaticity in the image plane located at the slits S_6. This beam-line will be designed for 10 Tm , but, for good dispersion matching the dipole D_5 has to be designed with the same bending radius as D_1 - D_4 (11.25 m) . The separation quality is essentially the same as described in Sec. 5.1. To obtain efficient beam transfer, the phase space of the separated projectile fragments has to fit into the ESR for the transversal as well as for the longitudinal coordinates.

For the high-intensity SIS-beams the horizontal and vertical emittances are 20 and 10 π mm mrad respectively. These emittances match the ESR acceptance for beams with a momentum spread of $\pm$.5%. This means, only half of the momentum width of $\pm$ 1 % provided by the fragment separator is acceptable in the ESR. Additional losses due to the smaller phase-space acceptance of the ESR are caused by the emittance growth induced by the degrader of the momentum-loss achromat. (see Sect. 4.) It is noteworthy to recall that the separator can also be operated as a monochromator to reduce the momentum spread. In this case the horizontal emittance is enlarged by the same factor as the momentum spread is reduced. This possibility will be subject of further calculations and not discussed here.

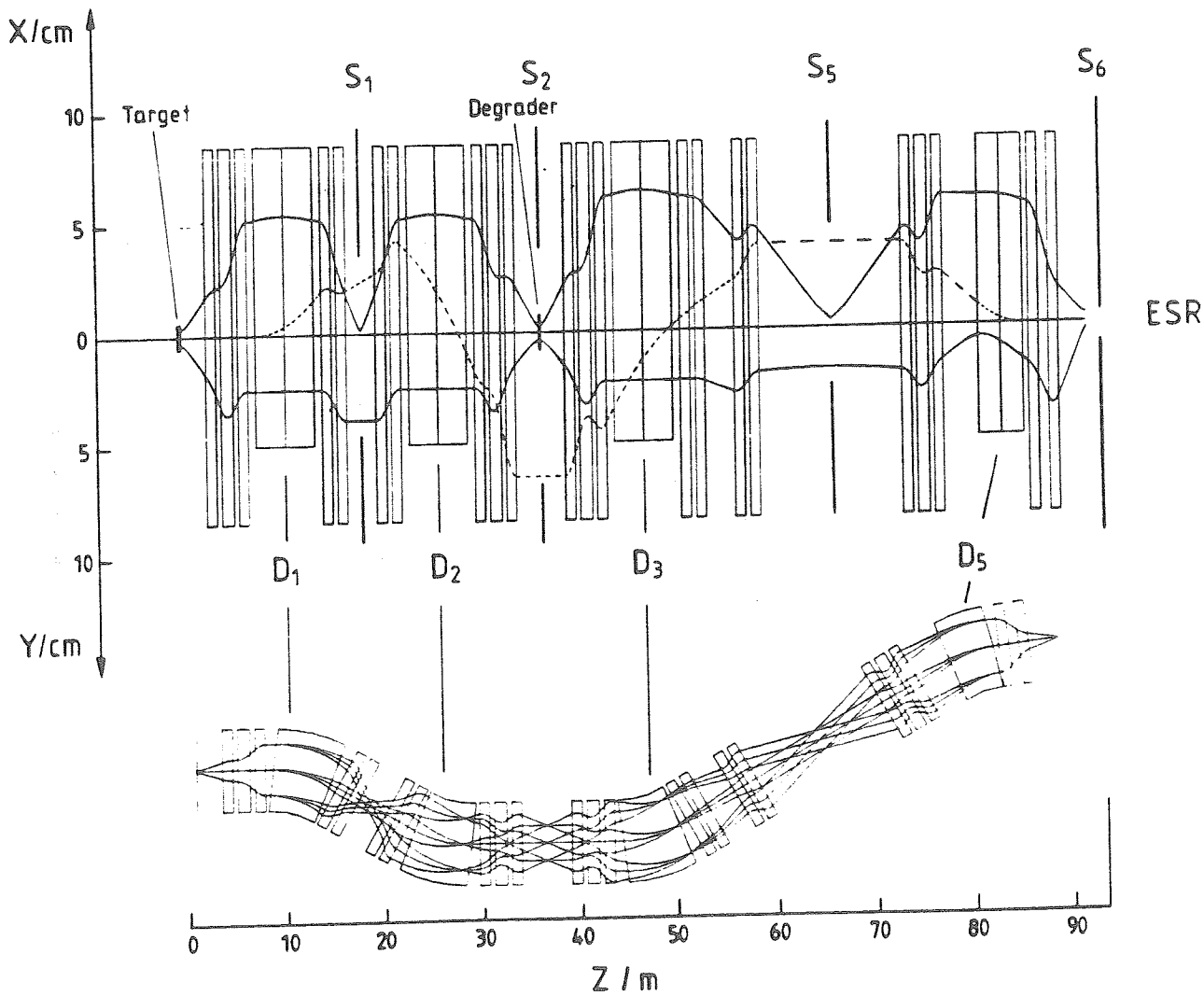

Fig. 5.2: Ion-optical layout for for the momentum-loss achromat to inject radioactive beams into the ESR.

		Stochastic pre-cooling	Electron cooling
Specific energy	[MeV/u]	500	30 - 560
Emittance reduction	[π mm•mrad]	20 → 2	2 → 0.1
Momentum width reduction	[%]	±0.5 → ±0.05	±0.05 → ±0.001
Cooling time	[s]	~1 s (10^8 ions)	0.2 - 0.6
Stacking time	[s]	- 0.02	-

Table 5.3: Parameters for stochastic and electron cooling

ESR and SIS are synchronized in rf, which has consequences for the stacking of bunches and will be discussed only briefly. If no degrader is inserted , two of the four bunches circulating in the SIS can be captured into rf-buckets in the ESR in one transfer cycle.This is due to the fact that the circumference of the ESR is half that of the SIS. If the beam penetrates through a degrader, the velocity is decreased and one has to choose a suitable asynchron rf and phase to capture the bunches. Estimates show that this is not a problem, if the degrader thicknesses are smaller than half the range of the selected fragments (the corresponding velocity loss is < 15%).

Before transferring the radioactive beam from the outer injection orbit to the inner storage orbit, stochastic pre-cooling should be applied. This cooling method is well suited to increase the phase-space density of low intensity beams with large emittances. The method is well suited for projectile fragments, before electron cooling can be efficiently applied as a second step on the stack orbit (see Table 5.3). The stochastic cooling system is designed for an ion velocity $\beta = 0.76$. At this velocity ions from the FRS will be essentially fully stripped, except for the very heaviest elements like uranium. The efficient storage of ions needs stochastic cooling, though it is possible to store also without pre-cooling ions on the expense of intensity and storage time. If lower energies down to about 100 MeV/u are demanded, e.g. beams of not completely stripped ions, stochastic cooling will not be available.

If stochastic pre-cooling is applied, the intensity of the stored beam may be increased by performing another injection pre-cooling cycle, while electrons may cool the stacked ions. Electron cooling is used to increase further the phase space density

of the stored ions to 0.1 π mm mrad and relative momentum spreads of $< 10^{-5}$. The cooling time amounts to 0.2 - 0.5 s .

The maximum number of ions that can be stored at a given energy depends critically on the emittance, momentum spread and time structure required [FRA86, HOF85] For example, at 556 MeV/u and $\Delta p/p \geq 1 \cdot 10^{-4}$. up to $9 \cdot 10^9$ $^{238}U^{92+}$ ions can be stored with transversal emittances of 1 π mm mrad. Values for other ion species can be deduced by scaling the uranium values with 36 A/q^2. The minimum number of particles that can be handled in the ring is given by the sensitivity limit of about 10^5 fully-stripped uranium ions in the ring.

The beam, which generally has at least been pre-cooled stochastically, can be decelerated to about 3 MeV/u within about 1.5 s and with a corresponding emittance growth of about a factor of 18. If necessary electron cooling can be applied down to about 30 MeV/u. At 3 MeV/u, $\Delta p/p \geq 2 \cdot 10^{-4}$. and $\varepsilon = 1$ π mm mrad, for example, the maximum number of stored ion is $2 \cdot 10^7$.

5.3 *Other Operation Modes of the Magnetic System*

The proposed magnetic system can also be operated as a high-resolution energy-loss spectrometer. Independent of the relatively large momentum spread of the incident projectile beam, precise measurements of energy transfers in nuclear reactions become possible [SCH64,GRO79]. Such a spectrometer consists of two stages with a dispersive focal plane in between where the target is positioned. For each target point, the momentum is well defined within the optical resolution of the separator. The second stage has just the inverse dispersion of the first part and focuses to first order all particles which suffer no nuclear energy loss at the optical axis. If the projectiles interact with target nuclei, the dispersion matching is no longer fulfilled and these particles of interest have a residual dispersion, causing a deflection which is characteristic for the Q-value. The elimination of the so-called effective dispersions due to kinematic effects and corrections of image aberrations are refinements to optimize the Q-value resolution. The targets used in the energy loss spectrometers are usually thin, so that the electronic energy losses can be neglected. The description of the ion-optical elements is identical to the one given for the momentum-loss achromat in Sec. 5.1 . The target is now at the degrader position where the primary beam is focused with a high dispersion. The size of the emittance accepted at the entrance of the spectrometer determines the achievable resolution .

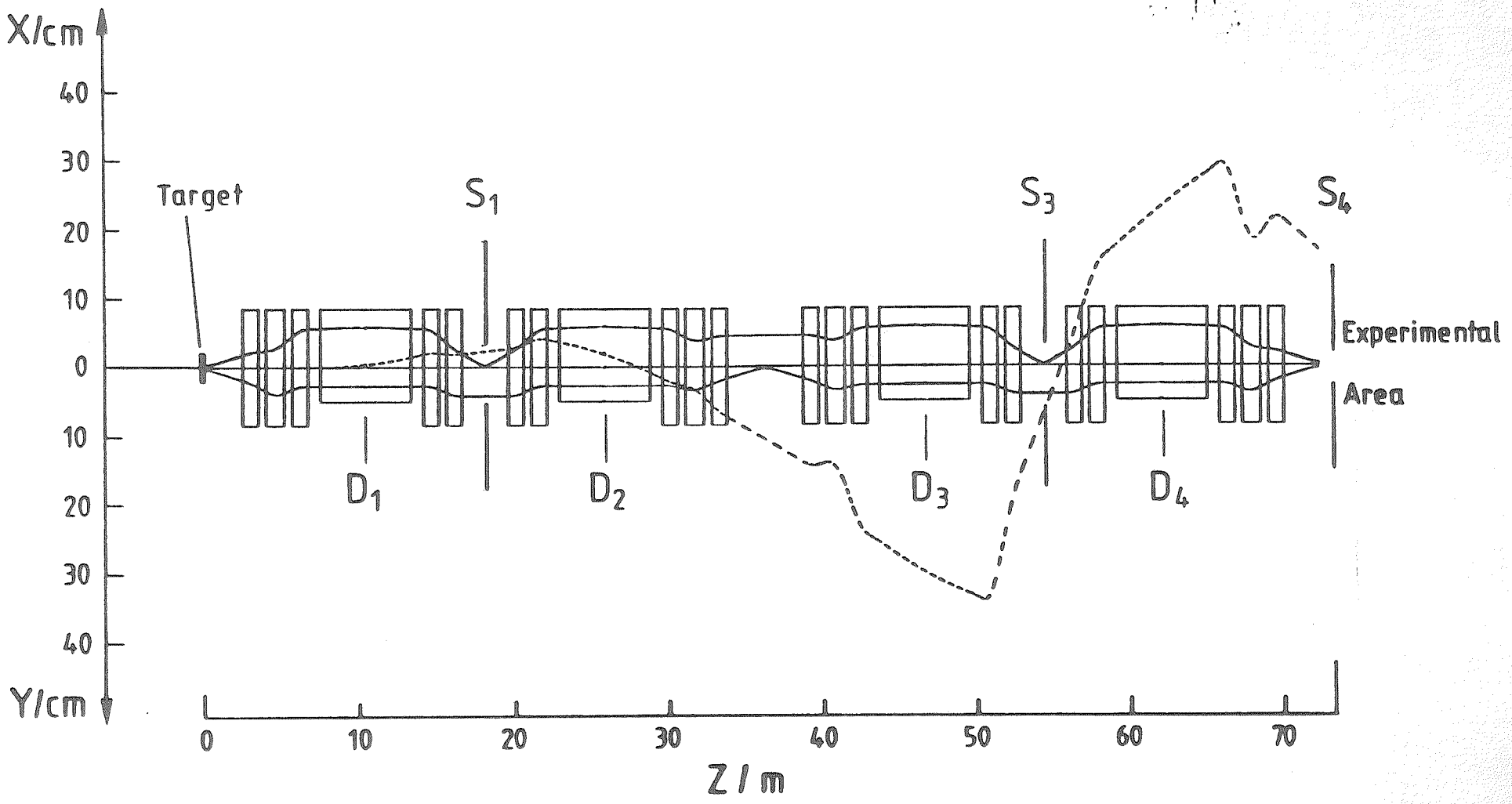

Fig. 5.3: Dispersive mode of the magnetic system

To first order the resolution is inverse proportional to the accepted emittance.(see Sec. 4.1) In the energy-loss mode the beam quality from SIS limits the resolution if the highest intensities are used. On the other hand we have restricted the beam intensity to a maximum of 5×10^8 particles/s, the expensive radiation shielding beeing planned only for this rate, so that the emittance can be decreased in order not to exceed this maximum rate and to improve the resolution.

As an energy-loss spectrometer and as the momentum-loss achromat, the magnetic system is always achromatic at the final focal plane. There might be applications, however, where a high resolution is required but not the achromatism. In this case the four sections of the magnet spectrometer are added in resolution. This means the total momentum resolution can easily be doubled. This dispersive mode of the magnetic system is shown in fig. 5.3 . In the symmetry plane we have not required the image condition but a parallel beam. For an emittance of 20 π mm mrad the momentum resolution is 3050 when the illuminated field volume is identical to the case presented in Sec. 5.1 for the momentum-loss achromat. All in all the magnetic device is very versatile and and can be used in many different experiments even though the design is optimized for the separation of radioactive beams.

5.4 Technical Layout

The projectile fragment separator is planned to be fully incorporated into the SIS-ESR system. Consequently, for the ion-optical components such as magnetic dipoles and quadrupoles including their power supplies, vacuum system, control system, beam diagnostics and scrapers SIS components are used and modified, only if necessary. Completely new technical developments are imperative for the target and the beam stop.

5.4.1 Target and Beam Stop

The intense beams of relativistic ions from the SIS require a detailed study of cooling and especially shielding against radioactive radiation from the target and the beam stop.

Table 5.4 shows examples of the heat deposition for Ne, Kr and U ions in different Be targets and in a beam stop. The thermal power in the targets ranges from 3 - 125

W which do not require special precautions for cooling in the case of the 1 g/cm^2-target .

The maximum heat deposited in the beam stop amounts to 380 W and is dissipated in a large volume, due to the large cross-section of the projectile beam and due to the large ranges of the relativistic ions slowed down in a beam stop. The heat can be removed by conventional cooling.

As far as radiation shielding is concerned, the beam stop is the main radiation source. In the target only 5 - 10 % of the beam will be converted into nuclear fragments. The produced high-energy neutron flux demands special precautions during the irradiation time. For example, if we assume the highest beam intensity of 5 x 10^{11}/s for 834 MeV/u Ne stopped in iron , roughly 10^{12} neutrons in the energy range 50 - 500 MeV are produced. Due to their large mean free path λ (λ(concrete) = 46 cm, λ(Fe) = 18 cm) thick shielding is needed. The angular distribution is peaked in forward direction and decreases roughly exponentially with larger angles. To shield the beam stop, a concrete wall of about 6 m thickness is necessary in the forward direction.

A special problem is that the primary beam will be dumped at different positions in the area between the second half of the first dipole $D_1$and the slits S_1 (see fig. 5.1), the positions depending on the chosen A/Z of the separated fragments .

After irradiation, a concrete wall of about 1m thickness should be sufficient to shield against β and γ radiation from the activated material in the beam stop. It is noteworthy to mention that in our layout an intesity exceeding $5 \cdot 10^8$ /s should never pass the slits S_1.

The target handling may cause radiation problems, since the low energetic target fragments are stopped in the target itself. For light targets, however, with $Z \leq 11$ such as beryllium, or carbon, no radioactive isotopes with half-lives between hours and years are produced except ^{7}Be. In fact, light targets will yield the highest production rates of projectile fragments and will thus be preferable. We will use only such materials in the target area and in the beam stop, which show the lowest activation. This will be subject to forthcoming engineering studies which have to cosider also target handling by remote control.

Table 5.4 : Heat deposition of Ne, Kr and U beams in Be targets and in the beam stop

projectiles	Ne	Kr	U
specific energy [GeV/u]	1	1	1
particle current [s^{-1}]	$1 \cdot 10^{11}$	10^{10}	10^{10}
power (1 g/cm^2 Be) [W]	3	4	25
power (5 g/cm^2 Be) [W]	15	19	125
power (beam stop) [W]	320	134	380

5.4.2 Dipoles and Quadrupoles

The deflection magnets and the quadrupoles are designed for the SIS beam rigidity of 18 Tm throughout the whole system, except for the beamline to the ESR, which is restricted to 10 Tm (see Sec. 5.1).

The dipoles are chosen to be H-type magnets due to the problems of the beam stop in dipole D_1 and due to the option to extract the beam through a hole in the yoke of the magnets D_1 and D_4. The cross section of a dipole magnet is shown in fig. 5.4 and its characteristic specifications are listed in table 5.5 . The dipoles are modified beam-line magnets used behind SIS and in the target hall. The differences are that they have larger pole face diameters and larger deflection angles. The magnets are laminated like the SIS-magnets, but will be used only in DC-operation. The maximum field is 1.6 T at a gap height of 98 mm and a usable field region of 170 mm for $\Delta B/B \leq 10^{-3}$. Dipole D_5 has the same bending radius needed for efficient dispersion matching as have all other dipoles.

The quadrupoles are identical to the SIS-quadrupoles except for their length, which is enlarged to meet the higher focusing powers needed in the fragment separator. The usable field region is 190 mm in diameter. Figure 5.5 shows the cross section of the quadrupole and its main specifications are given in table 5.6 .

For high transmission but lower resolution, a larger volume of the dipole and quadrupole fields (elliptical beam tubes) can be used, as given by the specifications above. The specifications of the power supplies and their control will be similar to the ones used for the SIS-ESR system.

Table 5.5: Specification of Dipole Magnets

Type	H
Quantity	4 / 1*
Deflection angle	30° / 23°*
Maximum field	1.6 T
Width for $\frac{\Delta B}{B} < 0.03$ %	2 x 95 mm
Bending radius	11.25 m
Gap height	98 mm
width	320 mm
Length (30°) without coils	5.823 m

*) for line to ESR

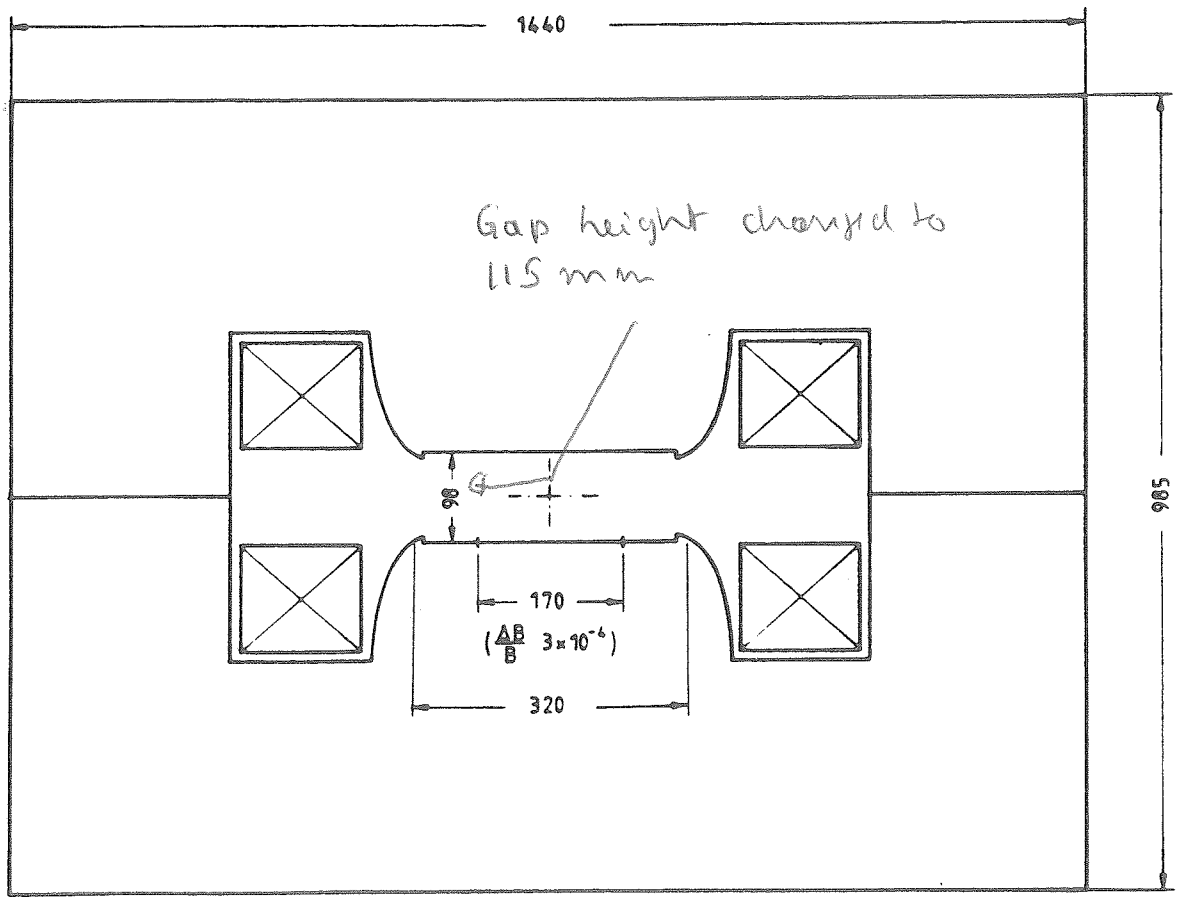

Fig. 5.4: Cross section of a H-type dipole magnet designed for FRS

Table 5.6: Specification of Quadrupoles

Quantity (length)	20(1 m) / 5(1.20 m)
max. Gradient	10 T/m
Aperture radius	85 mm
Region for $\Delta B'/B' < 0.1$ %	2 x 100 mm

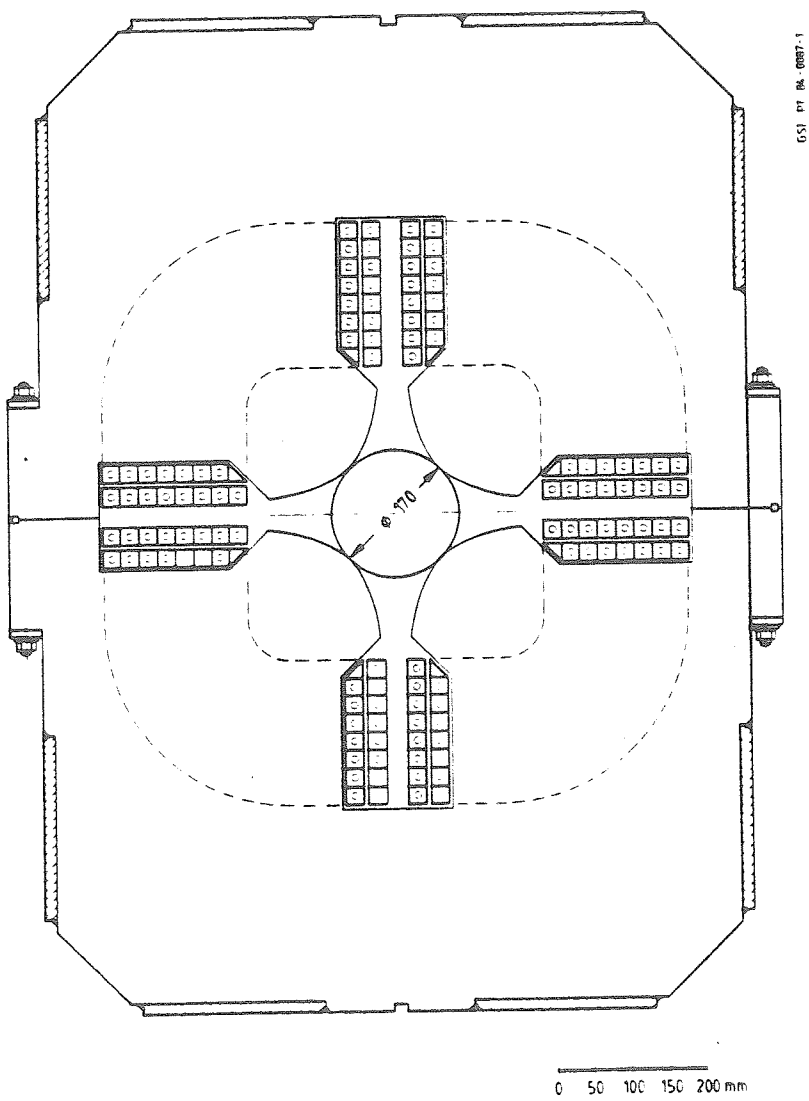

Fig. 5.5: Cross section of a quadrupole designed for FRS

5.4.3 Vacuum System

The vacuum system and control principally will resemble the SIS-ESR vacuum design, however the operation pressure will be close to 10^{-8} Torr for most experiments. This condition permits to insert most of the existing detector systems used in the past at the UNILAC. FRS vacuum will be separated from the accelerator and ESR vacuum by thin windows.

5.4.4 Beam Diagnostics and Scrapers

For high intensity beams the same diagnostics will be used as at SIS or in the beam line. For tracking of single particles in case of low-beam intensities, parallel plate counters will be installed at all focal planes.
The diaphragms and beam scrapers will be identical to those used in the accelerator beam lines. Howeverin order to minimize contamination of the separated beam due to nuclear interactions with the slit material, their exact shaping and the used material will be subject of forthcoming Monte-Carlo calculations.

5.4.5. Experimental Areas

At the projectile fragment separator (see Fig.1) there are two experimental areas:
Area 1 is located at the symmetry plane of the momentum-loss achromat where the absorber is located. For operation in the energy-loss mode, e.g., the target will be placed here. The space for detector systems in this target area is 5 m in beam direction and 7 m perpendicular to the beam. The maximum current is limited to 5 x 10^8/s. Small detectors may be placed at any slit position S_1-S_5.

Area 2, located at the final focal plane of the speparator is planned for investigations with secondary radioactive beams. This area is also essential for optimizing the separated radioactive beam before the injection into the ESR. A quadrupole triplet provides the necessary variability for the beam size and focal length. The beam energy is determined by the SIS-energy and the energy losses in target and degrader. Its upper limit corresponds to the 18 Tm beam rigidity of the separator. Generally the separated particles will be slowed down in absorbers and stopped in detectors for instance. The maximum beam current is the same as for area 1. The experimental area is 7 x 7 m^2.

For experiments in the ESR with radioactive beams, the experimental area 3, is used. Experimental area 4 is designed especially for experiments with beams of high phase-space density after cooling and for beams of variable energy in the range of 500 to 3 MeV/u, which have been decelerated in the ESR.

6. *Summary*

We described briefly the scientific motivations for the projectile fragment separator FRS and presented some data relevant for planning of experiments with this instrument. Particular emphasis was given to production rates of nuclear species, the separation method, the ion optical design and, to some extent, to the principles of the technical layout.

The proposed system is an achromat for separating projectile fragments,produced by SIS beams, and for injecting them into ESR. It consists of four ion-optical subsections, which allow a high versatility of operation modes. In the "momentum-loss" mode, the separator is used to separate unstable nuclei in A and Z. Our calculations showed that this separation is possible for all elements up to uranium. Other modes of operation are the energy-loss mode, or the high resolution mode with resolving powers $> 10^3$.

We are convinced that the instrument described in this proposal will become a versatile experimental tool for studies in a broad range of scientific topics. Especially the option to connect the projectile fragment separator with the storage ring will open a completely new field.

Acknowledgement

Discussions of ion-optical questions with K. L. Brown (SLAC), L. H. Harwood (MSU) and S. Martin (KFA) are gratefully acknowledged.

ABU 86 A.Y. Abul-Magd et al., Phys. Rev. ***C34*** (1986) 113

AHL 80 S. P. Ahlen, Rev. Mod. Phys. ***52*** (1980) 121

AHL 82 S. P. Ahlen, Phys. Rev. ***A25*** (1982) 1856

AND 87 S. Andriamonje et al., Nouvelles du GANIL ***19*** (1987) 9

ANG 86 N. Angert and P. Kienle eds., "10 years Uranium Beam at the UNILAC", GSI 86-19 (1986)

ANH 85 R. Anholt, Phys. Rev. ***A31***(1985) 3579

ANN 86 R. Anne et al., preprint GANIL P-86.24, submitted to Nucl. Instr. and Meth.

ARM 71 P. Armbruster et al., Nucl. Instr. and Meth. ***91*** (1971) 499

ARM 85 P. Armbruster, Ann. Rev. Nucl. Sci. ***35*** (1985) 135

BER 75 B.L. Berman, At.Data and Nucl.Data Tables ***15*** (1975) 319

BER 80 H. G. Berry, Proc. Workshop on Foundations of Relativistic Theory of Atomic Structure ***ANL-80-126*** (1980) (1986) 22

BET 76 H.D. Betz, Proc. Conf. "Atomic Physics in Nuclear Experiments", Haifa, 1976

BOH 48 N. Bohr, Dan. Mat. Fys. Medd. ***18*** No.8 (1948)

BOR 86 Bordeaux-GANIL-Orsay Collaboration, unpublished results.

BOS 86 U. Bosch et al., Phys. Lett. ***164B*** (1986) 22

BOS 86a F. Bosch, Proc. Int. Conf. on Nuclear Physics, Harrogate, 1986, in print

BRA 82 W. Brandt and M. Kitigawa, Phys. Rev. ***B25*** (1982) 5631

BRI 30 H.C. Brinkmann and H.A. Kramers, Proc. Acad. Sci. *33* (1930) 973

BRO 70 K.L.Brown, SLAC-Report No.91, Stanford (1970)

BRO 30 K.L. Brown et al. CERN Report *80-04* (1980), CERN Report *74-2* (1974)

CRO 77 E.A. Crouch, At.Data and Nucl.Data Tables *19* (1977) 417

CUM 78 J.B. Cumming et al., Phys. Rev. *C17* (1978) 1632; Phys. Rev. *C14* (1976) 1554; Phys. Rev. *C10* (1974) 739

CUR 86 M. S. Curtin et al., Phys. Rev. Lett. *56* (1986) 43

DUF 84 J. P. Dufour et al., Z. Phys. *A319* (1984) 237

DUF 86 J. P. Dufour et al., Z. Phys. *A234* (1986) 487, Nucl. Instr. and Meth. *A248* (1986) 267

FRA 83 B. Franczak,Proceedings of the Europhysics Conferenceon Computing in Accelerator Design and Operation , Berlin (1983)

FRA 86 B. Franzke, GSI-Report ESR-TN/86-01, 1986, and priv. comm.

FRA 85 B. Franzke, priv. comm., 1985

GIL 86 A. Gillibert et al., Phys. Lett. *176B* (1986) 317

GOL 74 A.S. Goldhaber, Phys. Lett. *53B* (1974) 306

GOU 84 H. Gould et al., Phys. Rev. Lett. *52* (1984) 180

GRO 79 E. Grorud et al., Rapport LNS/029 (1979)

GSI 84 "Die Ausbaupläne der GSI", GSI-Report, 1984

GUE 86 D. Guerreau, Journal de Physique *47* (1986) C4-207

GUI 85 D. Guillemaud-Mueller et al., Z. Phys. *A322* (1985) 415

HAN 87 P.G. Hansen and B. Jonson, priv. comm.

HIN 84 G. Hinderer et al., in Proc. "Arbeitstreffen über Experimente am geplanten Experimentierspeicherring ESR der GSI", Rauischholzhausen, eds. V. Metag et al., GSI-Report, 1984, p.149

HOF 82 S. Hofmann et al., Z. Phys. ***A305*** (1982) 111

HOF 85 I. Hofmann et al., GSI Report ***85-19***, 1985

HUB 84 G. Huber et al., in Proc. "Arbeitstreffen über Experimente am geplanten Experimentierspeicherring ESR der GSI", Rauischholzhausen, eds. V. Metag et al., GSI-Report, 1984, p.149

HUF 85 J. Hüfner, Phys. Reports ***125*** (1985) no.4, and references therein

JAC 72 J.D. Jackson and R.L. McCarthy, Phys. Rev. ***B6*** (1972) 4131

KAU 82 S.B. Kaufman et al., Phys.Rev. ***C26*** (1982) 2694

KLE 86 O. Klepper, in Proc. Int. Conf. on Weak and Electromagn. Interaction in Nuclei, Heidelberg, July 1986, H. V. Klapdor (ed.), Springer-Verlag, Berlin (1986) p.213

KOX 85 S. Kox et al., Phys. Lett. ***159B*** (1985) 15

KRA 86 K.-L. Kratz et al., Z. Phys. ***A325*** (1986) 489

LAN 58 J.E. Lannutti, S. Goldhaber, G. Goldhaber, W.W. Chupp, S. Giambuzzi, C. Marchi, G. Quarenti, A. Wataghin, Phys. Rev. ***109*** (1958) 2121

LAN 85 M. Langevin et al., Phys. Lett. ***150B*** (1985) 71

LAN 86 M. Langevin et al., Nucl. Phys. ***A455*** (1986) 149

LLA 83 J. Llacer, A. Chatterjee, E. K. Batho, J. A. Poskanzer, IEEE Trans. Nucl. Sci., Vol. NS-30 (1983) 617

LLA 84 J. Llacer, A. Chatterjee, E. L. Alpen, W. Saunders, S. Andreae, H. C. Jackson, IEEE Trans. on Medical Imaging Vol. M1-3 (1984) 80

LYO 66 V. L. Lyoboshitz et al., Sov. J. Nucl. Phys. *3* (1966) 420 , compare also R. Barden et al., UNILAC Experiment Proposal 401

MAR 62 J.B. Marcawitz and L. Ratner, Rev. Scient. Instr. ***33*** (1962) 552

MAR 67 J.B. Marion and B.A. Zimmerman, Nucl. Instr. Meth. ***51*** (1967) 93

MAR 86 R. Marrus et al., Phys. Rev. Lett. ***56*** (1985) 1683

MAY 85 W. Mayer et al., Phys. Lett. ***152B*** (1985) 162

MOL 48 G. Moliere, Z. Naturf. ***2A*** (1947) 133, ***3A*** (1948) 78

MUR 82 M. J. Murphy et al., Phys. Rev. Lett. ***49*** (1982) 455

NIG 59 B.P Nigam et al., Phys. Rev. ***115*** (1959) 491

NEU 69 G. Neuwirth et al., Z.Physik ***220*** (1969) 241

OLS 81 D.L. Olson et al., Phys.Rev. ***C24*** (1981) 1529

PAR 84 Particle Data Group, Rev. Mod. Phys. ***56*** No.2 (1984)

Phy Rev D50 (1994)

PEN 61 S.Penner, Rev.Sci.Instr. ***32*** (1961) 150

POR 79 N.T. Porile et al., Phys. Rev. ***C19*** (1979) 2288

POU 86 F. Pougheon et al., Europhys. Lett. ***2*** (1986) 505

PRA 73 R.H. Pratt et al., Rev. Mod. Phys. ***45*** (1973) 273

RUD 66 G. Rudstam, Z. Naturforsch. ***21a*** (1966) 1027

SAI 87 M. G. Saint-Laurent et al., submitted to Phys. Rev. Lett.

SCH 64 C. Schaerf et al. , Nucl. Instr. and Meth. ***30*** (1964) 359

SCH 81 D. Schardt et al., Nucl. Phys. ***A368*** (1981) 153

SCH 87 K.-H. Schmidt et al., preprint GSI 87-13 and to be published

SEK 86 T. Sekine et al., "The Beta Decay of ^{48}Mn: Gamow-Teller Quenching in fp-Shell Nuclei ", Nucl. Phys. ***A***, in print

SHE 86 B. Sherrill et al., Journal de Physique ***47*** (1986) C4-245

SIG 74 P. Sigmund and K.B. Winterbon, Nucl. Instr. Meth. *119* (1974) 541

STO 84 R.G. Stokstad, Comm.Nucl.Part.Phys. *13* (1984) 231

SYM 79 T. J.M. Symons et al., Phys. Rev. Lett. *42* (1979) 40

TAK 86 N. Takahashi priv. comm. 1986

TAN 85 I. Tanihata et al., Phys. Lett. *160B* (1985) 380

TAN 85a I. Tanihata et al., Phys. Rev. Lett. *55* (1985) 2676

THI83 F. K. Thielemann et al., Z. Phys. *A309* (1983) 301

TRI 85 The TRIUMF-ISOL Facility, TRIUMF-Report (1985)

TSC 68 C. Tschalär, Nucl. Instr. Meth. *64* (1968) 237

VIE 86 D. J. Viera et al., Phys. Rev. Lett. *26* (1986) 3253

VIY 79 Y.P. Viyogi et al., Phys. Rev. Lett. *42* (1979) 33

WAL 84 R. K. Wallace and S. E. Woosley, in High Energy Transients in Astrophysics, ed. S.E. Woosley, AIP Conf. Proc. No. 115, New York, p. 319

WES 79 G. D. Westfall et al., Phys. Rev. Lett. *43* (1979) 1859

WOL 67 H. Wollnik et al. , Nucl. Instr. and Meth. *38* (1967) 56

WOL 71 H. Wollnik et al., Nucl. Instr. and Meth. *95* (1971) 453

WOL 86 H. Wollnik et al., GSI Scientific Report 1985, p.372

WOU 86 J. M. Wouters et al., Preprint LA-UR-4184 (1986) and Nucl. Instr. and Methods, in press

ZIE 85 W. Ziegert et al., Phys. Rev. Lett. *55* (1985) 1935

ZIE 85a J.F. Ziegler et al., 'The Stopping and Range of Ions in Solids' Vol.1, Pergamon Press, New York (1985)